

THE SUN'S MERIDIONAL CIRCULATION AND INTERIOR MAGNETIC FIELD

T. S. WOOD¹, J. O. MCCASLIN², AND P. GARAUD¹

¹*Department of Applied Mathematics and Statistics, Baskin School of Engineering,
University of California Santa Cruz*

²*Department of Mechanical Engineering, College of Engineering and Applied Science,
University of Colorado Boulder*

tsw25@soe.ucsc.edu

ABSTRACT

To date, no self-consistent numerical simulation of the solar interior has succeeded in reproducing the observed thinness of the solar tachocline, and the persistence of uniform rotation beneath it. Although it is known that the uniform rotation can be explained by the presence of a global-scale confined magnetic field, numerical simulations have thus far failed to produce any solution where such a field remains confined against outward diffusion. We argue that the problem lies in the choice of parameters for which these numerical simulations have been performed. We construct a simple analytical magneto-hydrodynamic model of the solar interior and identify several distinct parameter regimes. For realistic solar parameter values, our results are in broad agreement with the tachocline model of Gough & McIntyre. In this regime, meridional flows driven at the base of the convection zone are of sufficient amplitude to hold back the interior magnetic field against diffusion. For the parameter values used in existing numerical simulations, on the other hand, we find that meridional flows are significantly weaker and, we argue, unable to confine the interior field. We propose a method for selecting parameter values in future numerical models.

Subject headings: MHD — Sun: interior — Sun: magnetic fields — Sun: rotation

1. INTRODUCTION

The differential rotation of the Sun's convective envelope terminates abruptly at the interface with the underlying radiative zone. The transition to uniform rotation takes

place across a stably-stratified shear layer known as the solar tachocline (Spiegel & Zahn 1992), whose thickness is at most a few percent of the Sun’s radius (Thompson et al. 1996; Kosovichev et al. 1997; Schou et al. 1998; Elliott & Gough 1999; Charbonneau et al. 1999; Basu & Antia 2003).

More than two decades after being first observed (Christensen-Dalsgaard & Schou 1988; Brown et al. 1989) a complete theory of the dynamics of the tachocline is still lacking. In particular, the thinness of the tachocline seems to be at odds with the known angular momentum transport properties of stratified rotating fluids, including advection by meridional circulations (Spiegel & Zahn 1992; Elliott 1997). Such circulations have a tendency to burrow into the radiative zone, transporting the convection zone’s angular momentum and thereby thickening the tachocline. In order for the tachocline to remain thin, some additional mechanism must be present that transports angular momentum latitudinally, and in such a way as to enforce uniform rotation. In addition, the angular velocity of the radiative zone inferred from helioseismology lies within the range of angular velocities observed at the solar surface, indicating that the spin-down of the surface by magnetic solar-wind drag (Schatzman 1962) has been communicated throughout the solar interior. This requires significant *vertical* transport of angular momentum. Again, the transport must be such as to enforce uniform rotation. We call such transport “frictional”, meaning down-gradient in angular velocity.

Several authors have argued that a combination of anisotropic turbulence and internal wave breaking can provide the required latitudinal and vertical angular momentum transport (e.g. Kumar & Quataert 1997; Zahn et al. 1997; Charbonnel & Talon 2005). However, both of these processes are known to have *anti*-frictional properties (e.g., McIntyre 1994; Gough & McIntyre 1998). On this basis, Gough & McIntyre argued that no non-magnetic model can explain the observed thinness of the tachocline and the persistence of uniform rotation within the radiative zone. On the other hand, the presence of a global-scale primordial magnetic field provides a natural explanation for the interior’s uniform rotation (e.g., Ferraro 1937; Mestel 1953; Mestel & Weiss 1987). Such a field enforces uniform rotation through the elasticity of the field lines imparted by magnetic tension. The thinness of the tachocline can also be explained by the presence of such a field, provided that the field lines are very nearly horizontal within the tachocline, so that angular momentum is transported from low to high latitudes by Maxwell stresses (Rüdiger & Kitchatinov 1997; Gough & McIntyre 1998; MacGregor & Charbonneau 1999; Wood & McIntyre 2011). We call such a field “confined”, meaning that the time-averaged mean field resides below the base of the convection zone. An unconfined field, on the other hand, would cause the convection zone’s differential rotation to propagate into the radiative zone (MacGregor & Charbonneau 1999; Garaud 2002; Brun & Zahn 2006).

To explain the confinement of the magnetic field, some process must be invoked to counteract the outward diffusion of the field throughout the Sun’s lifetime. Global-scale meridional flows that downwell from the convection zone into the radiative zone offer a possible mechanism for achieving magnetic field confinement — these are the same meridional flows that would lead to tachocline thickening in the absence of an interior magnetic field. This confinement mechanism was first suggested by Gough & McIntyre (1998) and later studied numerically by Garaud & Garaud (2008). The flows are generated by gyroscopic pumping in the convection zone, a mechanism which has been widely studied in the context of the Earth’s atmosphere, and more recently in an astrophysical context (McIntyre 2007; Garaud & Acevedo-Arreguin 2009; Garaud & Bodenheimer 2010). In brief, the same angular momentum transport by Reynolds stresses that gives rise to the differential rotation of the convection zone also drives a meridional circulation through angular momentum conservation (see Figure 1 of Garaud & Bodenheimer 2010). Such meridional circulations are a robust consequence of anisotropic angular momentum transport, as originally discussed by Kippenhahn (1963).

Although the Sun’s meridional flows can be observed directly at the solar surface, and inferred in the near-surface layers from local helioseismology (e.g., Haber et al. 2002; Zhao & Kosovichev 2004; Gizon et al. 2010), their amplitude and structure deeper within the solar interior is currently unknown. Theoretical and numerical models of the large-scale dynamics of the solar interior are required in order to establish whether the gyroscopically pumped circulation is strong enough, and penetrates deeply enough into the radiative zone, to confine the interior magnetic field and thereby explain the observed tachocline structure. Several such numerical studies have been performed (Garaud 2002; Brun & Zahn 2006; Garaud & Garaud 2008; Strugarek et al. 2011), but none has successfully reproduced the field-confinement scenario of Gough & McIntyre. However, since computing limitations prevent any numerical model from reaching true solar parameter values, this failure may simply reflect the fact that the numerical models are not in the parameter regime of relevance to the solar tachocline.

An alternative, analytical approach was proposed by Garaud & Brummell (2008), and further developed by Garaud & Acevedo-Arreguin (2009, hereafter GAA09). These preliminary models examined the amplitude and depth of penetration of global-scale meridional flows into the radiative zone in the absence of an interior magnetic field. In these non-magnetic models, the burrowing of the meridional flows was halted only by the presence of viscosity. In the steady state, the meridional mass flux was found to decay exponentially with depth below the radiative–convective interface on a lengthscale $\sim R_{\odot}/\sigma$, where R_{\odot} is

the solar radius and

$$\sigma = \frac{N}{\Omega_{\odot}} \sqrt{\frac{\nu}{\kappa}}. \quad (1)$$

Here ν is the viscosity, κ is the thermal diffusivity, N is the buoyancy frequency, and Ω_{\odot} is the mean solar rotation rate. This result shows how the burrowing tendency of the meridional flows is strengthened by rotation, and weakened by stable stratification and viscosity. Within the solar tachocline $\sigma < 1$, and so viscosity alone cannot prevent the meridional flows from burrowing into the radiative zone.

Garaud & Brummell (2008) found that the amplitude of the steady-state meridional flows in their model was sensitive not only to the value of σ , but also to conditions at the interface between the convective and radiative zones (see also Bretherton & Spiegel 1968). In a subsequent study, Garaud & Bodenheimer (2010) showed that the vertical mass flux below the radiative–convective interface can be quantified in terms of two constraints. The first constraint is that there must be stresses present in the radiative zone that overcome Taylor–Proudman balance. In the absence of such stresses, any meridional flows would have to be parallel to the rotation axis, which is not compatible with mass conservation. When such stresses are present, however, downwelling meridional flows are able to turn around and return to the convection zone — this is another example of gyroscopic pumping. Garaud & Bodenheimer called this the “mechanical” constraint.¹

The second constraint is due to the presence of stable stratification, which inhibits vertical flows; we call this the “thermal” constraint. Garaud & Bodenheimer (2010, hereafter GB10) found that this places an upper bound on the vertical flow velocity W of the form

$$|W| \leq \frac{R_{\odot}}{G t_{\text{ES}}} \quad (2)$$

where t_{ES} is the local Eddington–Sweet timescale,

$$t_{\text{ES}} = \left(\frac{N^2 R_{\odot}^2}{\Omega_{\odot}^2 \kappa} \right) \quad (3)$$

(e.g., Spiegel & Zahn 1992), and G is a dimensionless “geometrical” factor that depends on the details of the star’s internal structure.

The two constraints set two upper bounds for the meridional flow velocity, which then scales as the smaller of the two. In the case where the mechanical constraint is smaller,

¹ Since the mechanical constraint arises from the need to balance azimuthal forces, it applies only to the steady state. Transient meridional flows, such as those studied by Spiegel & Zahn, are not subject to this constraint and can be much stronger.

the meridional flow velocity depends on the nature of the stresses that overcome Taylor–Proudman balance. GB10 considered both laminar viscous stresses and turbulent Reynolds stresses in the convective cores of “lithium-dip” stars. In the present paper we consider magnetic stresses, which we argue are the dominant mechanism for angular momentum transport in the solar radiative zone. For simplicity, we neglect any turbulent stresses outside of the convection zone.

Following GAA09 and GB10 we use a linearized, steady-state, Cartesian model of the solar interior to study the interaction between meridional flows and an imposed confined magnetic field. In §2 we describe the Cartesian model and derive the governing equations. In §3 we present numerical and analytical solutions in the case where stratification is absent. We demonstrate a simple relationship between the structure and magnitude of the confined magnetic field and the pattern and amplitude of the meridional flows. In particular, we quantify the mechanical constraint from the confined magnetic field. In §4 we extend these results to the stratified case, recovering the thermal constraint mentioned above. We then discuss in §5 what insight the results of our simplified model provide into the nonlinear dynamics of the solar interior. In particular, we identify the various parameter regimes that occur in our model, and we discuss in which of these regimes the predicted meridional flows could plausibly bring about confinement of the magnetic field. The results show that great caution must be exerted when interpreting the results of numerical simulations that use non-solar values for the governing parameters, and provide guidance as to the design of future numerical simulations of the solar interior.

2. A Cartesian model

We use a similar model to that of GAA09. Although our model is intended as a simplified Cartesian analogue of the tachocline picture proposed by Gough & McIntyre (1998), it also goes beyond theirs in certain respects. We explicitly model the thermal and dynamical coupling between the convective and radiative zones, and are thus able to draw more quantitative conclusions concerning the role of this interaction in the global-scale solution. We also consider much wider numerical ranges in the governing parameters, and describe the structure of the solutions in several distinct parameter regimes. Our aim is to identify in which parameter regime, if any, the propagation of the differential rotation below the convection zone is restricted to a thin layer with a tachocline-like structure.

2.1. Model geometry

We measure distances in units of the solar radius, $R_\odot \simeq 7 \times 10^{10}$ cm, and velocities in units of $R_\odot \Omega_\odot$, where $\Omega_\odot \simeq 3 \times 10^{-6} \text{ s}^{-1}$ is the mean solar rotation rate, which we use as the inverse timescale. As illustrated in figure 1, the Cartesian coordinate system (x, y, z) is chosen such that x is the azimuthal coordinate, $y \in [0, \pi]$ is the latitudinal coordinate, and $z \in [0, 1]$ is the vertical coordinate. Although there is no precise equivalence between our Cartesian geometry and the spherical geometry of the solar interior, for the sake of interpretation we will take $y = 0$ and $y = \pi$ to be the “poles”, and $y = \pi/2$ to be the “equator”. The

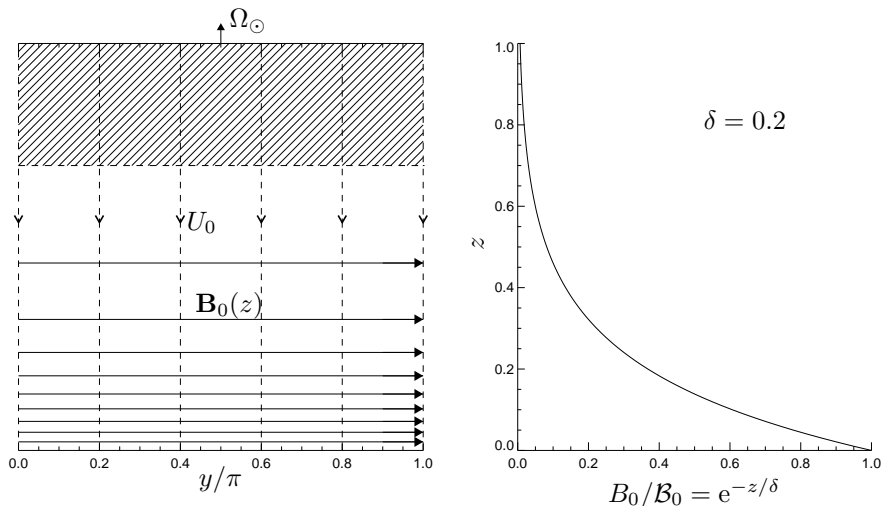


Fig. 1.— A meridional cross-section through the Cartesian model. The y and z axes represent latitude and altitude respectively. The shaded area marks the convection zone, where a forcing is applied to mimic the generation of differential rotation by turbulent stresses. The rotation axis is vertical. A global-scale magnetic field $\mathbf{B}_0(z) = \mathcal{B}_0 e^{-z/\delta} \hat{\mathbf{e}}_y$ is confined by uniform downwelling U_0 .

radiative–convective interface is at $z = h \simeq 0.7$, so that $h < z < 1$ represents the convection zone, and $0 < z < h$ represents the radiative zone.

2.2. Background state

The steady background state considered is depicted in figure 1. We model the transition between the convective and radiative zones by imposing a vertical profile for the dimensionless buoyancy frequency $n(z)$ with

$$n^2(z) = \frac{n_{\text{rz}}^2}{2} \left\{ 1 + \tanh \left(\frac{h - z}{\Delta} \right) \right\}, \quad (4)$$

so that $n = 0$ in the convection zone and $n = n_{rz} > 0$ in the radiative zone. The lengthscale Δ is introduced in order to ensure smoothness of the background state, which is necessary for numerical reasons. We may regard Δ as the thickness of the convective overshoot region at the base of the convection zone.

We impose a horizontal background magnetic field \mathbf{B}_0 of the form

$$\mathbf{B}_0 = B_0(z)\hat{\mathbf{e}}_y, \quad (5)$$

where $\hat{\mathbf{e}}_y$ is the unit vector in the y direction. In order to confine this field against ohmic diffusion, in the steady state, we must invoke a background meridional flow. The simplest case is that of uniform downwelling of dimensionless magnitude U_0 , and

$$B_0(z) = \mathcal{B}_0 e^{-z/\delta}, \quad (6)$$

where \mathcal{B}_0 is a constant and δ is the dimensionless lengthscale

$$\delta = \frac{\eta/(R_\odot^2 \Omega_\odot)}{U_0} = \frac{E_\eta}{U_0}. \quad (7)$$

Here η and E_η represent the magnetic diffusivity in dimensional and nondimensional units respectively; we call E_η the “magnetic Ekman number”. Although this background state cannot hold over all latitudes and depths within the solar interior (for reasons of mass conservation and solenoidality of \mathbf{B}_0), we hope that it offers a reasonable qualitative approximation to conditions within the tachocline at middle and high latitudes.

We note that \mathbf{B}_0 is not a force-free field since it has a non-constant magnetic pressure $B_0^2/(8\pi)$. However, the magnetic pressure can be balanced by a perturbation to the background gas pressure p_0 . Estimates of the strength of the Sun’s interior magnetic field typically lie within the range 10^{-3} – 10^3 gauss (e.g. Mestel & Weiss 1987; Gough & McIntyre 1998, see also §4.3). For field strengths in this range, the gas pressure far exceeds the magnetic pressure, and so the required perturbation is very small.

In what follows we consider linear, steady-state perturbations to this background state. The principle shortcoming of our model is, arguably, the artificial manner in which the magnetic field is confined to the interior, via the imposed downwelling U_0 . Magnetic confinement is thereby built into the model, and controlled by the parameters \mathcal{B}_0 and δ . This idealization is necessary to allow a linear study. A complete model of the tachocline would need to describe self-consistently the processes that act to confine the magnetic field, rather than treating it as part of the background. Such a model would necessarily be nonlinear, and awaits future numerical work. We note also that our Cartesian model cannot adequately describe the polar regions, where the effects of geometrical curvature become significant. The polar magnetic confinement problem has been studied in detail elsewhere (Wood & McIntyre 2011), and self-consistent, fully nonlinear solutions have been obtained.

2.3. Model equations

As in the studies of GAA09 and GB10 we do not model the turbulence in the convection zone in detail. Instead, we introduce a simple parametric model to describe its role in driving a large-scale differential rotation profile, and in enhancing the transport of heat. In the region $z \in [h, 1]$ we model the turbulent heat transport as a diffusive process, and we replace the divergence of the Reynolds stress with a forcing term that represents linear relaxation towards a prescribed rotation profile, which we choose to mimic the observed differential rotation of the solar convection zone.

For simplicity we also make the Boussinesq approximation (e.g. Spiegel & Veronis 1960), in which we neglect variations in the background pressure p_0 , density ρ_0 and temperature T_0 , and we neglect pressure perturbations in the equation of state. Although the Boussinesq approximation cannot be rigorously justified over the entirety of our domain, we do not expect this approximation to have a qualitative effect on our results. Indeed, we are interested primarily in solutions for which the meridional flows and differential rotation are confined to a thin, tachocline-like layer below the convection zone, within which the Boussinesq approximation should be quite accurate.

The nondimensional governing equations, linearized about the background state described in the previous section, are

$$2\hat{\mathbf{e}}_z \times \mathbf{u} = -\nabla p + T\hat{\mathbf{e}}_z + \Lambda e^{-z/\delta} \left[\frac{1}{\delta} \hat{\mathbf{e}}_x \times \mathbf{B} + (\nabla \times \mathbf{B}) \times \hat{\mathbf{e}}_y \right] + E_\nu \nabla^2 \mathbf{u} - \lambda(z)(\mathbf{u} - \mathbf{u}_{cz}) \quad (8)$$

$$n^2(z) w = E_\kappa \nabla \cdot (f(z) \nabla T) \quad (9)$$

$$0 = \nabla \times (\mathbf{u} \times e^{-z/\delta} \hat{\mathbf{e}}_y - \frac{1}{\delta} \hat{\mathbf{e}}_z \times \mathbf{B} - \nabla \times \mathbf{B}) \quad (10)$$

$$\nabla \cdot \mathbf{u} = 0 \quad (11)$$

$$\nabla \cdot \mathbf{B} = 0, \quad (12)$$

where $\mathbf{u} = (u_x, u_y, u_z)$ is the velocity perturbation, $\mathbf{B} = (b_x, b_y, b_z)$ is the perturbation to the magnetic field, p is the pressure perturbation, and T is the temperature perturbation. These equations have been scaled using $\rho_0 R_\odot^2 \Omega_\odot^2$ as the unit of pressure, $T_0 R_\odot \Omega_\odot^2 / g$ as the unit of temperature, and \mathcal{B}_0 / E_η as the unit of magnetic field strength. The following dimensionless parameters have been introduced:

$$\Lambda = \frac{\mathcal{B}_0^2}{4\pi\eta\rho_0\Omega_\odot}, \quad \text{the Elsasser number at } z = 0; \quad (13)$$

$$E_\nu = \frac{\nu}{R_\odot^2 \Omega_\odot}, \quad \text{the Ekman number;} \quad (14)$$

$$E_\kappa = \frac{\kappa}{R_\odot^2 \Omega_\odot}, \quad \text{the thermal Ekman number in the radiative interior.} \quad (15)$$

Note that the non-dimensionalized perturbation equations have no explicit dependence on the magnetic Ekman number E_η . However, because E_η has been used to scale the magnetic field, its value governs the magnitude of perturbations relative to the background field \mathbf{B}_0 .

The Elsasser number Λ is a measure of the relative magnitude of Lorentz forces compared to Coriolis forces. It is convenient to define also a local Elsasser number,

$$\Lambda_{\text{loc}}(z) = \frac{B_0^2(z)}{4\pi\eta\rho_0\Omega_\odot} \quad (16)$$

$$= \Lambda e^{-2z/\delta}, \quad (17)$$

in order to measure the relative magnitudes of these forces at each altitude z .

In both the momentum equation (8) and the thermal energy equation (9) we have neglected terms describing advection by the background downwelling U_0 . It can be shown that, in the results presented here, including these terms would produce only a small correction to the solutions. Neglecting these terms simplifies the analysis and reduces the dependence of the solutions on the artificially imposed flow U_0 .

The final term in the linearized momentum equation (8) describes a linear relaxation towards a prescribed rotation profile \mathbf{u}_{cz} . The dimensionless parameter λ , which determines the rate of relaxation, can be regarded as the inverse of the convective turnover timescale. This parameterization for the angular momentum transport by Reynolds stresses is similar to that used by Bretherton & Spiegel (1968), GAA09 and GB10. For simplicity, we assume that λ takes the constant value $1/\tau_c$ in the convection zone, and that the prescribed differential rotation \mathbf{u}_{cz} is sinusoidal in latitude. Following GAA09, we adopt the profiles

$$\mathbf{u}_{\text{cz}} = u_{\text{cz}}(z) e^{iky} \hat{\mathbf{e}}_x, \quad (18)$$

and

$$\lambda(z) = \frac{1}{2\tau_c} \left\{ 1 + \tanh\left(\frac{z-h}{\Delta}\right) \right\}, \quad (19)$$

where Δ is the same ‘‘overshoot’’ length as in equation (4). In the numerical results presented later we set $\tau_c = 0.1$ and $k = 2$, representing equatorial symmetry at the solar surface, and $u_{\text{cz}}(z)$ is taken to be linear in z . We show in appendix B that the flow below the convection zone is not very sensitive to the value of τ_c , or to the form of $u_{\text{cz}}(z)$, and that the results are easily extended to any particular $u_{\text{cz}}(z)$. This insensitivity to the choice of parameterization within the convection zone reflects the robustness of both the gyroscopic pumping mechanism and the burrowing tendency of meridional flows.

Finally, we model turbulent heat transport within the convection zone as an increase in the thermal diffusivity by a factor f relative to its laminar, microscopic value. We take

$$f(z) = 1 + \frac{f_0 - 1}{2} \left\{ 1 + \tanh\left(\frac{z-h}{\Delta}\right) \right\}, \quad (20)$$

so that $f = 1$ within the radiative zone and $f = f_0 \gg 1$ within the convection zone. Thermal perturbations at the radiative–convective interface are therefore communicated more efficiently into the convection zone than into the radiative zone. In the limit $f_0 \rightarrow \infty$ we expect the convection zone to become isothermal, which is equivalent to isentropic in our Boussinesq model. In the numerical results presented in §4 we take $f_0 = 10^6$. The physical significance of f_0 , and its effect on the solutions, is described in §4.3, below equation (72).

We assume that the viscosity ν and the magnetic diffusivity η retain their laminar, microscopic values throughout the solar interior. Introducing larger “turbulent” values for ν and η within the convection zone would not significantly affect the results we present here.

The perturbation fields must have the same sinusoidal dependence on y as the forcing term $\lambda(z) \mathbf{u}_{cz}$ in (8), and so we seek solutions of the form

$$q(\mathbf{y}, z) = \hat{q}(z) e^{iky}. \quad (21)$$

The perturbation equations (8)–(12) then become a system of ordinary differential equations for the perturbation amplitudes \hat{q} :

$$-2\hat{u}_y = ik\Lambda\hat{b}_x e^{-z/\delta} + E_\nu \left(\frac{d^2\hat{u}_x}{dz^2} - k^2\hat{u}_x \right) - \lambda(z)(\hat{u}_x - u_{cz}) \quad (22)$$

$$2\hat{u}_x = -ik\hat{p} - \frac{\Lambda}{\delta}\hat{b}_z e^{-z/\delta} + E_\nu \left(\frac{d^2\hat{u}_y}{dz^2} - k^2\hat{u}_y \right) - \lambda(z)\hat{u}_y \quad (23)$$

$$\frac{d\hat{p}}{dz} - \hat{T} = \frac{\Lambda}{\delta}\hat{b}_y e^{-z/\delta} + \Lambda \left(ik\hat{b}_z - \frac{d\hat{b}_y}{dz} \right) e^{-z/\delta} + E_\nu \left(\frac{d^2\hat{u}_z}{dz^2} - k^2\hat{u}_z \right) - \lambda(z)\hat{u}_z \quad (24)$$

$$0 = ik\hat{u}_x e^{-z/\delta} + \frac{1}{\delta} \frac{d\hat{b}_x}{dz} + \frac{d^2\hat{b}_x}{dz^2} - k^2\hat{b}_x \quad (25)$$

$$0 = ik\hat{u}_z e^{-z/\delta} + \frac{1}{\delta} \frac{d\hat{b}_z}{dz} + \frac{d^2\hat{b}_z}{dz^2} - k^2\hat{b}_z \quad (26)$$

$$\frac{n^2(z)}{E_\kappa} \hat{u}_z = \frac{d}{dz} \left(f(z) \frac{d\hat{T}}{dz} \right) - f(z)k^2\hat{T} \quad (27)$$

$$ik\hat{u}_y + \frac{d\hat{u}_z}{dz} = 0 \quad (28)$$

$$ik\hat{b}_y + \frac{d\hat{b}_z}{dz} = 0. \quad (29)$$

The system of equations (22)–(29) is solved numerically using a two-point boundary-value solver, given the boundary conditions listed below.

2.4. Boundary conditions

The upper and lower boundaries are modeled as impenetrable, (viscous) stress-free, isothermal and electrically insulating. That is, we impose

$$\left. \begin{aligned} \hat{u}_z &= 0 \\ \frac{d\hat{u}_x}{dz} &= 0 \\ \frac{d\hat{u}_y}{dz} &= 0 \\ \hat{T} &= 0 \\ \hat{b}_x &= 0 \end{aligned} \right\} \text{ at } z = 0 \text{ and } z = 1, \quad (30)$$

$$\frac{d\hat{b}_z}{dz} = k\hat{b}_z \text{ at } z = 0, \quad (31)$$

and
$$\frac{d\hat{b}_z}{dz} = -k\hat{b}_z \text{ at } z = 1. \quad (32)$$

Most of these boundary conditions have been selected for simplicity and convenience. In fact, the solutions turn out to be rather insensitive to the choice of boundary conditions in the parameter regime of interest, as we have verified by comparing solutions obtained with different sets of boundary conditions.

3. The Unstratified Case

3.1. Numerical exploration

In order to delineate the various physical effects present in the solutions, we begin by considering the unstratified case, $n_{rz} = 0$. Effects associated with stratification will be described in detail in §4.

A series of results is shown in figure 2. In the absence of any magnetic field (i.e., setting $\Lambda = 0$) we recover the non-magnetic, unstratified solution of GAA09 (see their figure 2). Since the lower boundary is stress-free, the differential rotation imposed within the convection zone is able to spread throughout the radiative zone, and establishes a state close to Taylor–Proudman balance. In this steady state the only meridional flows are those maintained by viscosity, and their magnitude scales with the Ekman number, E_ν . The meridional flows therefore become vanishingly weak in the limit $E_\nu \rightarrow 0$. When $\Lambda > 0$, on the other hand, the Lorentz force produces departures from Taylor–Proudman balance, and maintains a meridional flow even in the limit $E_\nu \rightarrow 0$ (figure 2b).

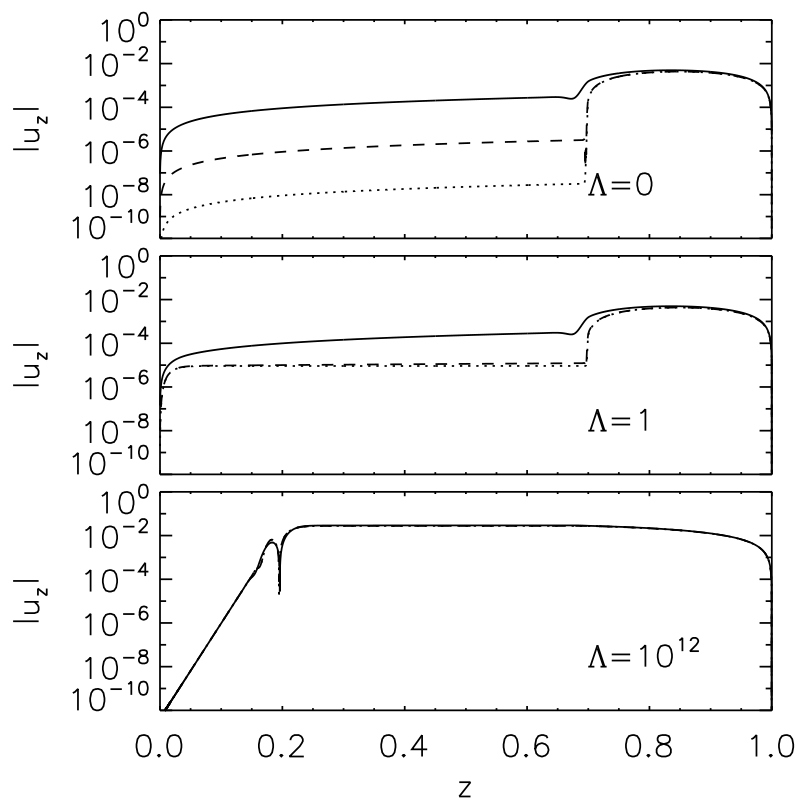


Fig. 2.— Profiles of vertical velocity \hat{u}_z for a series of unstratified solutions ($n_{rz} = 0$) with different magnetic field strengths and Ekman numbers. All the solutions have $u_{cz}(z) = 1 + (z - h)$ in (18), and $\Delta = 0.001$ and $\tau_c = 0.1$ in (19). The magnetic scaleheight, as defined by (7), is $\delta = 0.02$. Each panel shows the solutions for $E_\nu = 10^{-4}$ (solid line), $E_\nu = 10^{-6}$ (dashed line) and $E_\nu = 10^{-8}$ (dotted line).

For Λ of order unity, the Lorentz forces are most significant close to the lower boundary $z = 0$, within a boundary layer analogous to an Ekman–Hartmann layer. The structure of the boundary layer depends on the particular choice of boundary conditions at $z = 0$, including the magnetic boundary conditions. However, we have verified that the meridional flow outside the boundary layer is hardly affected by the choice of magnetic boundary conditions.

For $\Lambda \gg 1$ the radiative zone divides into two dynamically distinct regions, separated by a thin internal boundary layer at $z = z_0$, say (see figure 2c). The region above the boundary layer is close to Taylor–Proudman balance, with all components of \mathbf{u} independent of z , indicating that Lorentz forces are locally negligible (see figure 8a in §4.1 for plots of \hat{u}_x). In the region below the boundary layer, on the other hand, the Lorentz force is dominant, and all components of \mathbf{u} decay exponentially with depth. From here on we refer to these two regions as being “weakly magnetic” and “magnetically dominated” respectively. The boundary layer separating these two regions we call the “magnetic transition layer”. Since the flow within the magnetically dominated region decays exponentially with depth, the solution is insensitive to the choice of boundary conditions at $z = 0$.

The structure of the weakly magnetic and magnetically dominated regions is illustrated further in figure 3, which shows the meridional streamlines and magnetic field lines, as well as contours of the azimuthal components of the velocity and magnetic fields, in a vertical cross-section through a typical solution. Within the convection zone, the forcing that drives differential rotation also gyroscopically pumps a meridional flow. Below the base of the convection zone the forcing is switched off, and Taylor–Proudman balance is achieved. As a result, the meridional streamlines and angular velocity contours become aligned with the rotation axis, and a portion of the convection zone’s differential rotation extends into the radiative zone. This differential rotation winds up the magnetic field lines, producing a Lorentz torque whose amplitude increases exponentially with depth. Within the magnetic transition layer (here around $z_0 = 0.2$) the Lorentz torque is strong enough to overcome Taylor–Proudman balance, and gyroscopically pumps a meridional flow. The magnetic field lines are dragged upward where the flow is upwelling, $0 < y < \pi/2$, and pushed downward where the flow is downwelling, $\pi/2 < y < \pi$ (not shown in the figure). Below the transition layer, meridional flows and differential rotation are both strongly suppressed, and consequently perturbations to the magnetic field lines are smaller.

Figure 4 shows the result of increasing Λ still further. Over many orders of magnitude the only effect of increasing Λ is to raise the position of the magnetic transition layer, shrinking the vertical extent of the weakly magnetic region. The dynamics within the convection zone remain unaffected until the point at which the transition layer meets the base of the convection zone.

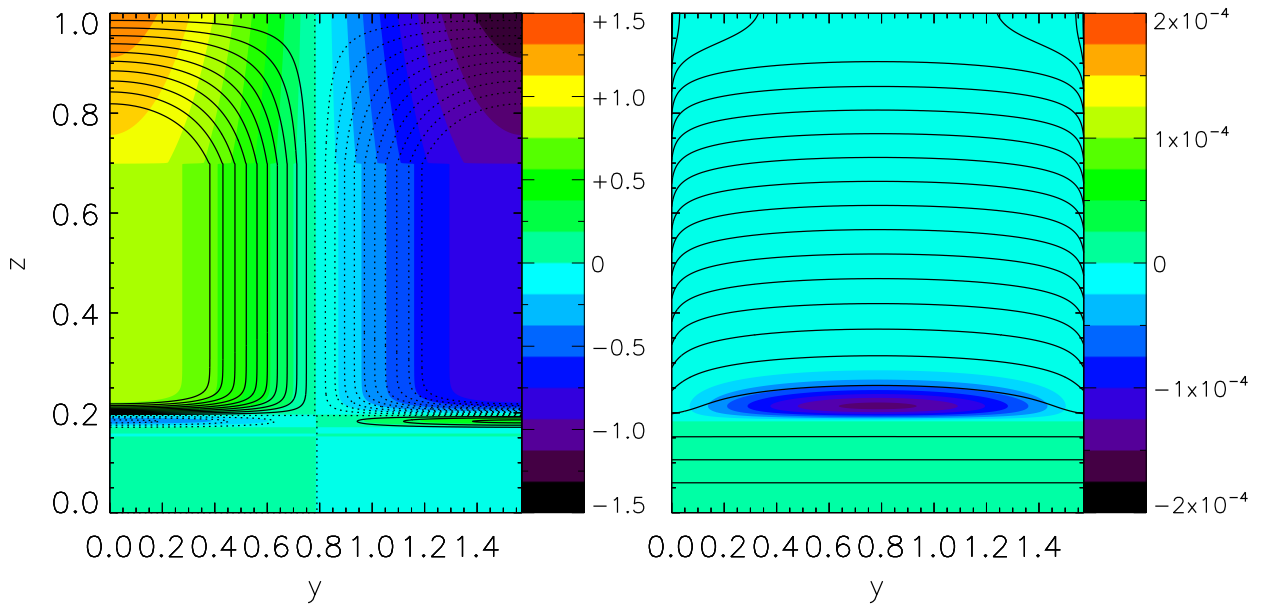


Fig. 3.— Meridional cross-section through the solution in figure 2 with $\Lambda = 10^{12}$ and $E_\nu = 10^{-8}$. The left panel shows the azimuthal velocity in color, overlaid with selected meridional streamlines (solid lines for anticlockwise flow, dotted lines for clockwise flow). The right panel shows lines of the poloidal magnetic field, including the background field \mathbf{B}_0 , assuming a magnetic Ekman number of $E_\eta = 10^{-4}$. Although field lines have been drawn at regular vertical intervals, the magnetic field strength decays exponentially with height. The color scale shows $b_x(x, y)/\mathcal{B}_0$.

It is obviously of interest to identify the factors determining the location of the magnetic transition layer. We anticipate that this transition occurs where the local Elsasser number Λ_{loc} , defined in (17), takes a critical value. We therefore expect the vertical position of the transition layer, z_0 , to follow a law of the form

$$z_0 = \text{const.} + \frac{1}{2}\delta \ln \Lambda \quad (33)$$

as Λ is increased, where the constant depends on the aforementioned critical value of Λ_{loc} . It is readily verified from figure 4 that z_0 does indeed follow such a law. In the following sections we analyze the structure of the solutions in detail in order to determine both the critical value of Λ_{loc} and the amplitude of the gyroscopically pumped meridional flow below the convection zone.

3.2. Analytical solution

In order to understand the results presented in §3.1 more quantitatively, we now derive approximate analytical solutions of the governing equations. In §3.2.1 we derive a boundary-

layer solution for the magnetic transition layer. In §3.2.2 we use that boundary-layer solution to construct a global analytical solution.

3.2.1. Transition layer solution

We seek to describe the transition layer between the weakly magnetic and magnetically dominated regions of the flow. Since this transition occurs below the base of the convection zone we may neglect the terms in the momentum equation involving λ . Based on the numerical solutions shown above, we anticipate that the thickness of the transition layer is of the same order as δ , the scaleheight of the background magnetic field. Since $\delta \ll 1/k$, we make the boundary-layer approximation

$$\left(\frac{d^2}{dz^2} - k^2 \right) \simeq \frac{d^2}{dz^2}. \quad (34)$$

We also neglect viscosity, i.e., we set $E_\nu = 0$. It can be verified *a posteriori* that viscosity plays no significant role in the dynamics of the transition layer provided that δ is much larger than the Ekman length, that is, provided that

$$\delta \gg E_\nu^{1/2}. \quad (35)$$

This condition is easily satisfied in the solar interior, where $E_\nu \simeq 10^{-15}$.

With these approximations, the governing equations (22)–(29) reduce to the following set:

$$-2\hat{u}_y = ik\Lambda\hat{b}_x e^{-z/\delta} \quad (36)$$

$$2\hat{u}_x = -ik\hat{p} - \frac{\Lambda}{\delta}\hat{b}_z e^{-z/\delta} \quad (37)$$

$$\frac{d\hat{p}}{dz} = \frac{\Lambda}{\delta}\hat{b}_y e^{-z/\delta} - \Lambda\frac{d\hat{b}_y}{dz} e^{-z/\delta} \quad (38)$$

$$0 = ik\hat{u}_x e^{-z/\delta} + \frac{1}{\delta}\frac{d\hat{b}_x}{dz} + \frac{d^2\hat{b}_x}{dz^2} \quad (39)$$

$$0 = ik\hat{u}_z e^{-z/\delta} + \frac{1}{\delta}\frac{d\hat{b}_z}{dz} + \frac{d^2\hat{b}_z}{dz^2} \quad (40)$$

$$ik\hat{u}_y + \frac{d\hat{u}_z}{dz} = 0 \quad (41)$$

$$ik\hat{b}_y + \frac{d\hat{b}_z}{dz} = 0. \quad (42)$$

We show in appendix A that these can be combined into a single equation for \hat{u}_z :

$$\left(\frac{d}{dz} - \frac{2}{\delta}\right) \left[\left(e^{z/\delta} \frac{d}{dz}\right)^4 + \frac{1}{4}k^4\Lambda^2 \right] \hat{u}_z = 0. \quad (43)$$

From inspection of (43) we deduce that the vertical position of the transition layer, z_0 , is given by

$$\begin{aligned} (e^{z_0/\delta}/\delta)^4 &= \frac{1}{4}k^4\Lambda^2 \\ \Rightarrow z_0 &= \delta \ln \left(k\delta/\sqrt{2}\right) + \frac{1}{2}\delta \ln \Lambda, \end{aligned} \quad (44)$$

which is consistent with (33). Furthermore, this expression shows that the transition layer is located where the local Elsasser number Λ_{loc} , defined by (17), takes the critical value $2/(k\delta)^2$. This corresponds to a critical magnetic field strength

$$B_{\text{crit}} = \frac{\sqrt{8\pi\eta\rho_0\Omega_\odot}}{k\delta} \simeq 40 \left(\frac{\eta}{\eta_\odot}\right)^{1/2} \left(\frac{0.001}{\delta}\right) \text{ G}, \quad (45)$$

where $\rho_0 \simeq 0.2 \text{ g cm}^{-3}$ and $\eta_\odot \simeq 400 \text{ cm}^2\text{s}^{-1}$.

We seek the solution to (43) that has the correct behavior in both the weakly magnetic region, for $z - z_0 \gg \delta$, and the magnetically dominated region, for $z - z_0 \ll -\delta$. In particular, the solution must match onto the differential rotation, $\hat{u}_x = u_t$ say, in the region immediately above the transition layer. Here, and subsequently, we use a subscript “t” to refer to the region immediately above the transition layer, which is also the bottom of the weakly magnetic region. We show in appendix A that the unique solution with the required properties is

$$\hat{u}_z = ik\delta u_t \left[I_1(\zeta) - \frac{\pi}{2} \text{Re} \left\{ \exp \left(-\frac{1+i}{\sqrt{2}}\zeta \right) \right\} \right], \quad (46)$$

where $\zeta = \exp((z_0 - z)/\delta)$, and I_1 is the integral

$$I_1(\zeta) = \int_0^\infty e^{-\zeta s} \frac{s ds}{1 + s^4}. \quad (47)$$

The weakly magnetic and magnetically dominated regions correspond to $\zeta \ll 1$ and $\zeta \gg 1$ respectively.

Figure 5 shows the vertical profiles of \hat{u}_z and \hat{u}_x , in the vicinity of the magnetic transition layer, from the same numerical solution shown in figure 3. Also shown are their analytical counterparts, (46) and the corresponding analytical profile of \hat{u}_x .

Within the magnetically dominated region, where $\zeta \gg 1$, the flow is exponentially weak. From (46) we find that

$$\hat{u}_z \sim \frac{ik\delta u_t}{\zeta^2} = ik\delta u_t \exp \left(\frac{2(z - z_0)}{\delta} \right). \quad (48)$$

Within the weakly magnetic region, where $\zeta \ll 1$, \hat{u}_z tends to a constant, w_t say, as expected from the Taylor–Proudman constraint. Specifically,

$$w_t = \hat{u}_z|_{\zeta=0} = -i\frac{\pi}{4}k\delta u_t. \quad (49)$$

The vertical mass flux within the weakly magnetic region is therefore tied to the differential rotation via the magnetic transition layer.

3.2.2. Global solution

We now use the relation (49) derived from our transition-layer solution to construct an approximate analytical solution for the global flow. In this way we derive an explicit relation between the constant vertical velocity w_t within the weakly magnetic region and the prescribed differential rotation $u_{cz}(z)$ within the convection zone. To construct the global solution, we must also match the flow within the weakly magnetic region, $z_0 < z < h$, to the flow within the convection zone, $h < z < 1$. The matching procedure is similar to that employed by GB10, and is described in appendix B. Here we present only the result for w_t .

In the absence of stratification, $n_{rz} = 0$, we find that w_t is given by

$$w_t = \frac{-i\bar{u}_{cz}}{\frac{kd}{2\tau_c} \coth\left(\frac{1-h}{d}\right) + \frac{4}{\pi k\delta}} \quad (50)$$

where d is the “convective” lengthscale²

$$d = \frac{\sqrt{4\tau_c^2 + 1}}{k} \quad (51)$$

and where \bar{u}_{cz} is a weighted average of the forcing in the convection zone,

$$\bar{u}_{cz} = \frac{\int_h^1 dz u_{cz}(z) \cosh\left(\frac{1-z}{d}\right)}{\int_h^1 dz \cosh\left(\frac{1-z}{d}\right)}. \quad (52)$$

Since $d > 1/k > (1-h)$, the weight distribution in (52) is roughly uniform, and so \bar{u}_{cz} is numerically close to the vertical average of $u_{cz}(z)$ over the convection zone.

²The lengthscale d in this paper is equivalent to the lengthscale δ_{out} in GB10.

Figure 6 shows the vertical profiles of \hat{u}_z in a series of numerical solutions with various magnetic scaleheights δ . The bottom panel in figure 6 compares the value of \hat{u}_z in the weakly magnetic region to the value for w_t predicted by (50). The fit is excellent provided that the magnetic transition layer is located sufficiently far above the lower boundary, $z = 0$, and sufficiently far below the base of the convection zone, $z = h$. Using (44), these two conditions can be expressed as lower and upper bounds on Λ :

$$\frac{2}{(k\delta)^2} \ll \Lambda \ll \frac{2e^{2h/\delta}}{(k\delta)^2}. \quad (53)$$

3.3. Summary and discussion for the unstratified case

We have found that a confined magnetic field is able to halt the burrowing of the convection zone’s differential rotation into the radiative interior, provided that the magnetic field strength exceeds a critical value B_{crit} given by (45). Because the field strength in our model increases monotonically with depth, the radiative zone divides into an upper, weakly magnetic region, wherein $B_0(z) \ll B_{\text{crit}}$, and a lower, magnetically dominated region, wherein $B_0(z) \gg B_{\text{crit}}$. In the weakly magnetic region the flow is subject to the Taylor–Proudman constraint, and the differential rotation u_x is independent of z . In the magnetically dominated region the flow is subject to the Ferraro constraint, which suppresses both differential rotation and meridional flows. In our model $B_0(z)$ increases exponentially with depth on a fixed lengthscale δ , and so the transition between the weakly magnetic and magnetically dominated regions occurs across a layer of thickness $\simeq \delta$, within which $B_0 \simeq B_{\text{crit}}$.

The transition layer regulates the mass flux that downwells from the convection zone, as expressed by equation (49). This is closely related to the mechanical constraint mentioned in §1, and can be explained as follows. The latitudinal differential rotation below the base of the convection zone extends downward until it meets the transition layer, where it winds up the magnetic field lines, producing a Lorentz torque that overcomes Taylor–Proudman balance and gyroscopically pumps a meridional flow. In the steady state, the downwelling mass flux within the weakly magnetic region must be exactly that demanded by the transition layer, which is expressed by (49). An analogy can be made with the more familiar Ekman pumping that occurs in Ekman layers. Indeed, if the transition layer were replaced by an artificial frictional, impenetrable and non-magnetic horizontal boundary, then (49) would be replaced by the Ekman-pumping formula,

$$w_t = -\frac{1}{2}ik\delta_E u_t \quad (54)$$

(GAA09), where $\delta_E = E_\nu^{1/2}$ is the nondimensional Ekman-layer thickness. In the solutions

presented here we have $\delta \gg \delta_E$, and so the magnetic transition layer pumps much stronger meridional flows than would be pumped by an artificial Ekman layer.

The solutions we have found bear many similarities to the tachocline model originally proposed by Gough & McIntyre (1998). In particular, we have a differentially rotating region below the base of the convection zone, which we might call the tachocline, and a thin magnetic boundary layer at the base of this region, which Gough & McIntyre called the “tachopause”. The entire region below the tachopause is held in uniform rotation by the confined magnetic field. However, an obvious shortcoming of our unstratified solutions is that the “tachocline” has no vertical shear, quite unlike the solar tachocline. In the Gough & McIntyre model, the tachocline’s vertical shear is explained by the presence of stable stratification, via the thermal-wind relation. In the following sections we reintroduce stratification into our model, in order to better approximate conditions within the solar tachocline.

4. The Stratified Case

The importance of stratification in our model can be measured in terms of the dimensionless parameter n_{rz}^2/E_κ , which appears on the left-hand side of (27). In fact, it follows from equation (2) that

$$\frac{n_{rz}^2}{E_\kappa} = \Omega_\odot t_{ES}, \quad (55)$$

so n_{rz}^2/E_κ is precisely the dimensionless local Eddington–Sweet timescale. In what follows we also use $\sigma = n_{rz}(E_\nu/E_\kappa)^{1/2}$ as a measure of the stratification. As mentioned in §1, this parameter is particularly relevant in cases where buoyancy and viscosity both contribute to the balance of forces. All the numerical solutions presented in this section have $E_\nu = 10^{-8}$, and so the parameters n_{rz}^2/E_κ and σ contain equivalent information.

4.1. Numerical exploration

We begin again by exploring the behavior of the solutions of (22)–(29) with varying governing parameters. In figure 7 we show the vertical profiles of \hat{u}_z in a series of numerical solutions with increasing stratification, measured in terms of σ . When σ is sufficiently small, $\lesssim 10^{-3}$, the profiles are indistinguishable from one another and from the unstratified solution, which has $\sigma = 0$. The same is true for the profiles of \hat{u}_x in these solutions, which are shown in figure 8a. In particular, the weakly magnetic region ($z_0 < z < h$) remains in Taylor–Proudman balance. We refer to all such cases as “unstratified”, since any effects due to stratification are negligible.

As σ is increased beyond 10^{-3} we observe a reduction in \hat{u}_z in the weakly magnetic region (see figure 7). At the same time, the jump in \hat{u}_x across the magnetic transition layer drops almost to zero, and instead $\hat{u}_x(z)$ rises smoothly and monotonically between z_0 and h , indicating that thermal-wind balance has been established within the weakly magnetic region. For brevity, and because of the obvious similarity with the model of Gough & McIntyre (1998), from here on we refer to the weakly magnetic region and magnetic transition layer in such cases as the “tachocline” and “tachopause” respectively.

We find that cases with significant stratification can be further categorized as being either “weakly stratified”, “moderately stratified”, or “strongly stratified”. These three regimes are now described in turn.

4.1.1. *The strongly stratified regime*

In common with Garaud & Brummell (2008) and GAA09, we find that the strength of the meridional flow \hat{u}_z decays exponentially with depth below the convection zone on the vertical scale $1/(k\sigma)$. If σ is sufficiently large, $\gtrsim 1$, then this vertical scale is smaller than the tachocline thickness, and so meridional flows gyroscopically pumped at the base of the convection zone are halted by a combination of buoyancy and viscous forces before reaching the tachopause. Following the terminology introduced by GAA09 we refer to such cases as “strongly stratified”. Even with strong stratification, the differential rotation \hat{u}_x driven in the convection zone still spreads into the radiative interior (figure 8a), but by viscous diffusion rather than by the burrowing of meridional circulations. The differential rotation winds up the magnetic field lines much as in the unstratified cases described in §3, producing a Lorentz torque within the tachopause that gyroscopically pumps a meridional flow. Part of that meridional flow is launched upward into the tachocline, where its strength decays with height on the lengthscale $1/(k\sigma)$. The strongly stratified solutions therefore have meridional circulations within two distinct horizontal layers, at the top and bottom of the tachocline.

4.1.2. *The weakly stratified and moderately stratified regimes*

Figure 8b shows vertical profiles of \hat{T} from the same series of solutions shown in figure 7. In all cases with $\sigma \lesssim 10^{-1}$ we find that there is little variation in the temperature field \hat{T} or its vertical gradient $\partial\hat{T}/\partial z$ across the tachopause. However, in cases with $\sigma \gtrsim 10^{-1}$ we observe a significant change in the temperature gradient at $z = z_0$, indicating that the flow within the tachopause contributes to the global-scale thermal equilibrium. We refer to cases

with $10^{-3} \lesssim \sigma \lesssim 10^{-1}$ as “weakly stratified”, and cases with $10^{-1} \lesssim \sigma \lesssim 1$ as “moderately stratified”.

Figure 9 illustrates how the mass flux in the tachocline varies with the strength of the interior magnetic field in the weakly and moderately stratified regimes. As in the unstratified case, we find that the position of the magnetic transition layer moves upwards as Λ increases, in a manner which is more-or-less independent of σ . However, in contrast with the unstratified case, the strength of the meridional flow within the tachocline varies with Λ (cf. figure 4). For increasing values of Λ , the meridional flow becomes stronger as the tachocline becomes thinner. This result has implications for the solar tachocline, as will be discussed in §4.2.2.

Figure 10 shows meridional cross-sections through two solutions in the weakly and strongly stratified regimes. As mentioned in §1, the solar tachocline has $\sigma \simeq 0.2$ – 0.4 (GAA09), and therefore is not strongly stratified in the sense used here. We anticipate that either the weakly stratified or the moderately stratified regime offers the best approximation to the dynamics of the tachocline. In the following sections we analyze these two regimes in detail in order to quantify more precisely the parameter ranges over which they apply.

4.2. Analytical solution

We proceed, as in §3.2, by deriving an analytical boundary-layer solution for the tachopause, which can then be used to construct a global analytical solution. In order to simplify the analysis we will neglect the viscous terms in the equations, and so our analytical solutions cannot be applied in the strongly stratified regime.

4.2.1. The tachopause

In the unstratified, weakly stratified and moderately stratified solutions presented in figure 8b, the temperature field $\hat{T}(z)$ is roughly constant in the region $z - z_0 = O(\delta)$. (Recall that the moderately stratified cases are characterized by a jump in $d\hat{T}/dz$, rather than \hat{T} .) We can therefore analyze the structure of the tachopause in all three regimes simultaneously by approximating \hat{T} as a constant, T_t . As in §3.2.1 we neglect viscosity and make the boundary-layer approximation (34). We then recover equations (36)–(42) exactly, except

that (38) is replaced by

$$\frac{d\hat{p}}{dz} - T_t = \frac{\Lambda}{\delta} \hat{b}_y e^{-z/\delta} - \Lambda \frac{d\hat{b}_y}{dz} e^{-z/\delta}. \quad (56)$$

Within the tachocline, where $z - z_0 \gg \delta$, all the terms involving Λ are negligible, and so we have

$$\hat{u}_y \simeq 0 \quad (57)$$

$$2\hat{u}_x \simeq -ik\hat{p} \quad (58)$$

$$\frac{d\hat{p}}{dz} - T_t \simeq 0 \quad (59)$$

$$ik\hat{u}_y + \frac{d\hat{u}_z}{dz} \simeq 0. \quad (60)$$

We deduce that

$$\left. \begin{array}{l} \hat{u}_x \sim u_t - \frac{1}{2}ikT_t(z - z_0) \\ \hat{u}_y \rightarrow 0 \\ \hat{u}_z \rightarrow w_t \end{array} \right\} \text{ as } \frac{(z - z_0)}{\delta} \rightarrow +\infty, \quad (61)$$

where the constants u_t and w_t represent the values of \hat{u}_x and \hat{u}_z immediately above the tachopause, or equivalently, at the bottom of the tachocline.

As in §3.2.1 we can combine all of our boundary-layer equations into a single equation for \hat{u}_z :

$$\left(\frac{d}{dz} - \frac{2}{\delta} \right) \left[\left(e^{z/\delta} \frac{d}{dz} \right)^4 + \frac{1}{4}k^4\Lambda^2 \right] \hat{u}_z = \frac{k^4\Lambda}{4\delta} T_t e^{2z/\delta}. \quad (62)$$

In appendix A we show that the unique solution of (62) that satisfies (61) is

$$\begin{aligned} \hat{u}_z = ik\delta u_t & \left[I_1(\zeta) - \frac{\pi}{2} \operatorname{Re} \left\{ \exp \left(-\frac{1+i}{\sqrt{2}}\zeta \right) \right\} \right] \\ & + \frac{1}{2}k^2\delta^2 T_t \left[I_2(\zeta) - \frac{\pi}{2} \operatorname{Re} \left\{ (\gamma - i\frac{\pi}{4}) \exp \left(-\frac{1+i}{\sqrt{2}}\zeta \right) \right\} \right] \end{aligned} \quad (63)$$

where γ is the Euler–Mascheroni constant, $\gamma = 0.577\dots$, $\zeta = \exp((z_0 - z)/\delta)$, as in §3.2.1, and

$$I_1(\zeta) = \int_0^\infty \frac{s ds}{e^{\zeta s}} \frac{1}{1 + s^4}, \quad (64)$$

$$I_2(\zeta) = \int_0^\infty \frac{s ds}{e^{\zeta s}} \frac{\gamma + \ln s}{1 + s^4}. \quad (65)$$

Figure 11 shows the vertical profiles of \hat{u}_z and \hat{u}_x , and their analytical counterparts, from the same numerical solution shown in the top panel of figure 10.

From (63) we deduce a relation between the constants T_t , u_t , and w_t ,

$$w_t = \hat{u}_z|_{\zeta=0} = -\frac{i\pi}{4}k\delta u_t - \frac{\gamma\pi}{8}k^2\delta^2 T_t. \quad (66)$$

It can be verified that (66) holds, to reasonable accuracy, in each of the solutions presented in §4.1. Furthermore, in each case the term in (66) involving T_t is found to be negligible, and so (66) reduces to the relation (49) derived for the unstratified transition layer. The vertical mass flux within the tachocline is therefore tied to the differential rotation much as in the unstratified case described in §3.

We can also use (63) to quantify the role of the tachopause in the global-scale heat flow. Within the tachopause the thermal energy equation (27) becomes

$$\frac{n_{rz}^2}{E_\kappa} \hat{u}_z = \frac{d^2 \hat{T}}{dz^2} \quad (67)$$

after making the boundary-layer approximation (34). Therefore the change in the vertical temperature gradient across the tachopause is

$$\begin{aligned} \left[\frac{d\hat{T}}{dz} \right]_{z=z_0-\delta}^{z=z_0+\delta} &= \frac{n_{rz}^2}{E_\kappa} \int_{z_0-\delta}^{z_0+\delta} \hat{u}_z dz \\ &\sim \frac{n_{rz}^2}{E_\kappa} w_t \delta. \end{aligned} \quad (68)$$

The transition between the weakly stratified and moderately stratified regimes occurs when (68) is of comparable magnitude to the temperature gradient within the tachocline (see figure 8b).

4.2.2. Global solution

We can use the relations (66) and (68) to construct an approximate analytical solution for the global flow. The details of the solution procedure are set out in appendix B. We find that the vertical velocity w_t in the tachocline is

$$w_t = \frac{-i\bar{u}_{cz}}{\frac{kd}{2\tau_c} \coth\left(\frac{1-h}{d}\right) + \frac{4}{\pi k\delta} + \frac{n_{rz}^2}{2k^2 E_\kappa} [G_1 + G_2 - G_3]}, \quad (69)$$

which reduces to equation (50) in the absence of stratification, $n_{rz} = 0$. The dimensionless “geometrical” factors G_1 , G_2 and G_3 are given by (B30)–(B32) in the weakly stratified

regime and by (B33)–(B35) in the moderately stratified regime. We refer to these factors as geometrical because of their dependence on the tachocline thickness, $D = h - z_0$. However, they also depend on f_0 , the thermal diffusivity enhancement factor defined in (20). Moreover, G_2 depends on the lengthscale d defined by (51), and hence on the forcing timescale τ_c .

We can use (69) to quantify the boundary between the unstratified and weakly stratified regimes identified in §4.1. This boundary is located where the term in the denominator of (69) involving n_{rz} becomes as large as the term involving δ . In general the geometrical factors are of order unity or smaller, and so the unstratified regime corresponds to

$$\frac{n_{rz}^2}{E_\kappa} \lesssim k/\delta. \quad (70)$$

For the solutions in figures 7 and 8, which have $E_\nu = 10^{-8}$, $k = 2$, and $\delta = 0.02$, this condition is equivalent to $\sigma \lesssim 10^{-3}$, in good agreement with the numerical results.

The boundary between the weakly and moderately stratified regimes occurs where the change in the temperature gradient across the tachopause, given by (68), becomes comparable to the temperature gradient within the tachocline. As described in appendix B, this condition can be expressed approximately as

$$\frac{n_{rz}^2}{E_\kappa} \simeq 1/(k\delta^3). \quad (71)$$

For the solutions in figures 7 and 8 this condition is equivalent to $\sigma \simeq 0.025$, which is consistent with (although somewhat smaller than) the value $\sigma \simeq 0.1$ found in the numerical solutions.

The bottom panels of figures 7 and 9 verify that the analytical prediction (69) for the vertical flow velocity in the tachocline agrees with the numerical results described earlier. Since viscosity was neglected in the derivation of (69) this good agreement demonstrates that the weakly stratified and moderately stratified regimes are both inviscid, that is, viscous forces do not play a significant role in the dynamics. In particular, the solutions do not have an Ekman layer at the radiative–convective interface, $z = h$. We believe that the existence of such an Ekman layer in some previous studies (e.g. Gilman & Miesch 2004; Rüdiger et al. 2005; Garaud & Brummell 2008) arises from the treatment of the interface in those studies. In all the results presented here, the change in buoyancy frequency n at the interface is smoothed over a lengthscale Δ , representing the depth of convective overshoot, that greatly exceeds the Ekman length $\delta_E = E_\nu^{1/2}$. In the other studies just mentioned, the interface was modelled either as an upper boundary with a fixed differential rotation, or by a change in n over a lengthscale $\ll \delta_E$. Although the precise thickness of the Sun’s overshoot layer is not known, it is surely thicker than the Ekman length $(\nu/\Omega_\odot)^{1/2} \simeq 30$ m, and so we argue that there is no Ekman layer in the solar tachocline.

4.3. Physical interpretation and discussion of the stratified results

It is useful to compare the expression for w_t given by (69) to the corresponding expression derived by GB10 for meridional circulations pumped between the outer and inner convective zones of young lithium-dip stars (see their equation (23)). As in their model, the magnitude of the circulation induced by the convective stresses is proportional to \bar{u}_{cz} , a weighted average of the prescribed differential rotation in the convection zone. It is then moderated by whichever term in the denominator of (69) is largest. The first term is always of order unity or larger, and so w_t can never exceed \bar{u}_{cz} in magnitude. The second term, involving δ , limits w_t to a flow rate which can be accommodated by the magnetic transition layer, as discussed in §3; this is an example of the “mechanical” constraint mentioned in §1. The third term, involving n_{rz} , represents the thermal constraint described in §1. This constraint limits w_t to a flow rate for which the temperature perturbations created by the advection of the background stratification can be balanced by thermal diffusion, thereby maintaining thermal equilibrium.

The expression for w_t given by (69) can be simplified considerably in the parameter regime appropriate to the solar interior. In the solar tachocline we have $n_{rz}^2/E_\kappa \simeq 8 \times 10^{13}$, and so the tachocline is not in the unstratified regime according to the criterion (70) unless the tachopause is unrealistically thin, $\delta \lesssim 10^{-13}$. Therefore the denominator of (69) is dominated by the thermal term. The weakly stratified and moderately stratified regimes, according to (71), correspond to $\delta \lesssim 10^{-5}$ and $\delta \gtrsim 10^{-5}$ respectively. The solar tachocline could plausibly be in either of these regimes. Fortunately, it can be shown that G_1 , G_2 and G_3 follow similar scaling laws in either case, differing only by factors of order unity. We can therefore consider both regimes simultaneously.

We expect the tachopause to be much thinner than the tachocline, $\delta \ll D$, which is itself much thinner than the solar radius, $D \ll 1$. Under these conditions it can be shown that

$$G_1/G_2 \sim f_0(kD)^2 \tag{72}$$

and

$$G_1/G_3 \sim D/\delta \gg 1 \tag{73}$$

in both the weakly and moderately stratified regimes. The right-hand side of (72) corresponds to the ratio of the thermal adjustment timescales in the tachocline and convection zone respectively. In the solar tachocline, thermal adjustment by radiative diffusion has a timescale of about 10^4 years, whereas the thermal adjustment timescale in the convection zone, estimated using mixing-length theory, is about 1 year. We therefore assume $f_0(kD)^2 \gg 1$, in which case $G_1 \gg G_2, G_3$. This same assumption was made implicitly in the models of Spiegel & Zahn (1992) and Gough & McIntyre (1998), in both of which the top of the tachocline was assumed to be isothermal. Under this assumption we find that

$G_1 \sim (kD)^3$, and so (69) becomes

$$w_t \sim -i\bar{u}_{cz} \left(\frac{2E_\kappa}{n_{rz}^2 k D^3} \right). \quad (74)$$

We note that w_t then depends only indirectly on the structure of the interior magnetic field, via the tachocline thickness D . The dependence of w_t on D can be understood physically as a consequence of thermal equilibrium and thermal-wind balance, as first discussed by Gough & McIntyre (1998) (see also McIntyre 2007, p 194). Since the vertical shear across the tachocline is of order \bar{u}_{cz}/D , thermal-wind balance implies that there must be a temperature perturbation \hat{T} of order $\bar{u}_{cz}/(kD)$. Such a perturbation cannot persist within the convection zone, where heat is transported very efficiently by convective motions, but can persist within the tachocline, where heat transport is less efficient. In the tachocline, temperature perturbations diffuse at the rate E_κ/D^2 , and thermal equilibrium therefore requires that $n_{rz}^2 w_t \sim E_\kappa \hat{T}/D^2 \sim (E_\kappa/D^2)(\bar{u}_{cz}/(kD))$, from which (74) follows immediately. Using order-of-magnitude estimates for the tachocline thickness, $D \simeq 0.01$, and differential rotation, $\bar{u}_{cz} \simeq 0.1$, as well as $n_{rz}^2/E_\kappa \simeq 8 \times 10^{13}$, we find from (74) that $w_t \sim 10^{-9}$, dimensionally $w_t \sim 10^{-4} \text{ cm s}^{-1}$. We note, however, that this result is rather sensitive to the tachocline thickness D , which is not well constrained by observations.

Our model therefore recovers Gough & McIntyre’s scaling for the meridional flow within the tachocline, and goes further by clarifying the physical assumptions under which that scaling is derived, and by identifying the necessary conditions for those assumptions to hold. Under more general conditions, the meridional flow strength w_t is given by (69), and (74) should be regarded instead as an approximate upper bound on w_t . The more general formula (69) may be of relevance to the interiors of solar-type stars that are more weakly stratified, or that have thicker tachoclines.

Of course, we must be careful when applying the results of our idealized model, with its artificially confined magnetic field, to the solar interior, or indeed to the interiors of other stars. However, since the formula for w_t given by (74) has no explicit dependence on the structure of the background magnetic field \mathbf{B}_0 , we argue that this result should hold for more general, less artificial field configurations than that considered here. Moreover, the physical processes that give rise to (74) will be present in any self-consistent model of the solar interior, and so (74) ought to be a robust result under solar-like conditions.

We now ask whether the meridional flows predicted by (74) would be of sufficient magnitude to confine an interior magnetic field against outward diffusion. In our idealized model, the interior field \mathbf{B}_0 is confined by an artificially imposed downwelling U_0 . A first approximation to the nonlinear magnetic confinement problem can be obtained by setting $U_0 = |w_t|$.

Using (7), we can then relate the tachopause thickness δ to the tachocline thickness D :

$$\frac{E_\eta}{\delta} \sim \bar{u}_{cz} \frac{2E_\kappa}{n_{rz}^2 k D^3} \quad (75)$$

$$\Rightarrow \delta \sim \frac{E_\eta n_{rz}^2 k}{E_\kappa 2\bar{u}_{cz}} D^3. \quad (76)$$

This expression is equivalent to equation (7) in Gough & McIntyre (1998).

We can now predict the strength of the magnetic field within the tachopause, B_t say, using equation (45). Here, our model differs significantly from that of Gough & McIntyre. They assumed that thermal-wind balance would hold within the tachopause, as well as in the bulk of the tachocline, and as a result the thickness of the tachopause in their model, δ_{GM} say, was tied to the strength of the stable stratification. They found that

$$\delta_{GM} = \left(\frac{2E_\kappa}{k^4 n_{rz}^2 \Lambda_t} \right)^{1/6} \quad (77)$$

where $\Lambda_t = \Lambda_{loc}(z_0) = B_t^2 / (4\pi\eta\rho_0\Omega_\odot)$ is the Elsasser number within the tachopause. In our model, on the other hand, the Lorentz force within the tachopause overcomes thermal-wind balance, and we find that

$$\delta = \left(\frac{2}{k^2 \Lambda_t} \right)^{1/2} \quad (78)$$

(see §3.2.1). Hence, whereas Gough & McIntyre find a very strong dependence of B_t on D , namely $B_t \propto D^{-9}$ (see their equation (8)), we find by combining (76) and (78) that $B_t \propto D^{-3}$, and more precisely,

$$\frac{B_t^2}{4\pi\rho_0 R_\odot^2 \Omega_\odot^2} \sim \frac{8\bar{u}_{cz}^2 E_\kappa^2}{n_{rz}^4 k^4 D^6 E_\eta}. \quad (79)$$

Taking $k = 2$, $n_{rz}^2/E_\kappa \simeq 8 \times 10^{13}$, and $E_\eta \simeq 3 \times 10^{-14}$, we find

$$\frac{B_t^2}{4\pi\rho_0 R_\odot^2 \Omega_\odot^2} \sim 3 \times 10^{-5} \left(\frac{\bar{u}_{cz}}{0.1} \right)^2 \left(\frac{D}{0.01} \right)^{-6} \quad (80)$$

$$\Rightarrow B_t \sim 10^3 \left(\frac{\bar{u}_{cz}}{0.1} \right) \left(\frac{D}{0.01} \right)^{-3} \text{ G}. \quad (81)$$

This estimate is rather higher than the ~ 1 G field predicted by Gough & McIntyre. We note that torsional Alfvénic oscillations of a ~ 1000 G field could explain the 1.3 year oscillation detected in the tachocline’s angular velocity (Gough 2000).

4.4. Guidance for the selection of parameters in numerical models

In recent years there have been several attempts to achieve magnetic field confinement in self-consistent, nonlinear, global numerical models of the solar interior. Various approaches have been taken, including axisymmetric steady-state calculations (Garaud & Garaud 2008), as well as two-dimensional and three-dimensional time-dependent simulations (Garaud & Rogers 2007; Rogers & MacGregor 2011; Strugarek et al. 2011). However, none of these numerical models has so far obtained solutions that are satisfactorily close to solar observations, and none has achieved magnetic confinement over an extended range of latitudes. These failures have led some to conclude that the magnetic confinement picture of Gough & McIntyre is unworkable. However, the analytical results presented here suggest that magnetic confinement by meridional flows *can* be achieved in the parameter regime appropriate to the solar tachocline. We can also use our results (a) to explain the lack of magnetic confinement in existing numerical models, and (b) to guide parameter selection for future models.

As shown in §4.1, the amplitude of meridional flows within the radiative interior decreases monotonically as the stratification is increased. Moreover, in a time-dependent model, the timescale for the burrowing of the flows, given by (3), increases with stratification. In the strongly stratified regime, with $\sigma \gtrsim 1$, the burrowing of meridional flows is even slower than viscous diffusion. But if $\sigma < 1$, as is the case in the tachocline, then the meridional flows are approximately inviscid. When modelling the solar interior, it is common practice to impose a rotation rate and stratification profile that are close to solar, in order to ensure a realistic separation between the dynamical timescales. The viscous, thermal, and magnetic diffusivities (ν, κ, η) are then made as small as possible, subject to computational constraints. However, adopting this strategy does not guarantee that $\sigma < 1$. Indeed, if the ratio of buoyancy and rotational frequencies n_{rz} is chosen to match the true tachocline value, then the condition $\sigma < 1$ requires the Prandtl number ν/κ to be very small,

$$\nu/\kappa < \frac{1}{n_{rz}^2} \simeq 10^{-5}. \quad (82)$$

This condition is satisfied in the solar interior, but is beyond the reach of current numerical simulations, which instead typically have a Prandtl number much closer to unity, in order to reduce the numerical stiffness of the equations. This places such simulations in the strongly stratified regime in which (a) meridional flow velocity decays exponentially with depth below the convection zone, and (b) viscous stresses make a significant dynamical contribution, even if the Ekman number is small, i.e. even if $E_\nu \ll 1$.

The numerical difficulty is, in fact, rather easily avoided by imposing a weaker stratification, and thus allowing for a larger Prandtl number. For example, if $n_{rz} = 10$ then (82) requires only that $\nu/\kappa < 10^{-2}$, which is readily achievable numerically. We then expect

the meridional flow velocity in the tachocline to scale as (74), provided that the radiative–convective interface remains approximately isothermal (see discussion below (72)).

A further numerical difficulty is the need to resolve both the thin tachocline and the thinner tachopause. This difficulty can be alleviated by allowing the tachocline to be somewhat thicker than is observed in the Sun.³ According to (76), to obtain a tachopause of thickness $\delta = 0.01$ and a tachocline of thickness $D = 0.1$, for example, we require

$$\frac{E_\eta n_{rz}^2 k}{E_\kappa 2\bar{u}_{cz}} \sim 10. \quad (83)$$

If we choose $n_{rz} = 10$, as suggested above, as well as $\bar{u}_{cz} \simeq 0.1$ and $k = 2$, then this requires a diffusivity ratio $\eta/\kappa = E_\eta/E_\kappa \sim 10^{-2}$. The strength of the interior magnetic field must then be chosen in accordance with (79), which requires

$$\frac{B_t^2}{4\pi\rho_0 R_\odot^2 \Omega_\odot^2} \sim 50E_\kappa. \quad (84)$$

Finally, we must ensure that the Ekman length $E_\nu^{1/2}$ is smaller than $\delta = 0.01$.

All of the constraints just described can be satisfied by choosing $E_\kappa = 10^{-3}$, $E_\eta = 10^{-5}$, and $E_\nu = 10^{-6}$, as well as $n_{rz} = 10$ and $B_t^2/(4\pi\rho_0) = 0.05R_\odot^2\Omega_\odot^2$. These parameter values should be numerically achievable; in fact, the suggested values of E_κ , E_η , and E_ν are very similar to those used by Brun & Zahn (2006).

5. Discussion and Conclusion

Following the failure of several recent attempts to recreate the Gough & McIntyre tachocline scenario in global numerical models, our main goal in this work was to identify in what parameter regime, if any, the results of Gough & McIntyre apply. For this purpose we created a model of the tachocline that is sufficiently simple to have analytical solutions yet, we believe, incorporates enough of the relevant dynamics to yield quantitative predictions.

We have identified four distinct parameter regimes that occur in our results as the strength of the stratification is increased. For solar parameter values, the results lie in either

³The strength of the Sun’s stratification increases rapidly with depth below the convection zone. For models that use a solar-like vertical profile of n_{rz} , care must be taken to ensure that the condition $\sigma < 1$ holds throughout the tachocline.

the “weakly stratified” regime or the “moderately stratified” regime (see §4.1.2). In both of these regimes the strength of the meridional flow within the tachocline is determined by a combination of thermal equilibrium and thermal-wind balance, and follows the scaling predicted by Gough & McIntyre. With realistic tachocline parameters, the downwelling flow is of sufficient strength to confine an interior magnetic field across a thin boundary layer, and the thickness of the tachocline is related to the strength of the magnetic field by (81).

By contrast, all previous attempts to model the tachocline numerically have been performed in the “strongly” stratified regime, in which the burrowing of meridional flows is significantly reduced by viscosity. We believe that this explains the lack of field confinement in those models. To remedy the problem, we suggest an alternative set of numerically achievable parameters, which we predict will yield results that are much more consistent with solar observations.

This project was initiated during the ISIMA 2010 summer program, funded by the NSF CAREER grant 0847477, the France–Berkeley fund, the Institute of Geophysics and Planetary Physics, and the Center for the Origin, Dynamics and Evolution of Planets. We thank them for their support. P.G. and T.W. were also supported by NSF CAREER grant 0847477, and J.M. was supported by NCAR and the Geophysical Turbulence Program.

A. Analytical derivation of the transition-layer solution

The magnetic transition layer is described by equations (36)–(42), except that (38) is replaced by (56) in cases with stratification. After eliminating \hat{p} , \hat{u}_y , and \hat{b}_y , these reduce to

$$2\frac{d\hat{u}_z}{dz} = -k^2\Lambda\hat{b}_xe^{-z/\delta} \quad (\text{A1})$$

$$2\frac{d\hat{u}_x}{dz} = -ikT_t + \Lambda\left(\frac{1}{\delta^2}\hat{b}_z - \frac{d^2\hat{b}_z}{dz^2}\right)e^{-z/\delta} \quad (\text{A2})$$

$$0 = ik\hat{u}_xe^{-z/\delta} + \frac{1}{\delta}\frac{d\hat{b}_x}{dz} + \frac{d^2\hat{b}_x}{dz^2} \quad (\text{A3})$$

$$0 = ik\hat{u}_ze^{-z/\delta} + \frac{1}{\delta}\frac{d\hat{b}_z}{dz} + \frac{d^2\hat{b}_z}{dz^2}. \quad (\text{A4})$$

We now define a new variable $\zeta = \exp((z_0 - z)/\delta)$, with z_0 given by (44), and so the domain $-\infty < (z - z_0)/\delta < +\infty$ maps onto $\infty > \zeta > 0$. When written in terms of ζ , equations

(A1)–(A4) become

$$\frac{d\hat{u}_z}{d\zeta} = k\sqrt{\frac{\Lambda}{2}}\hat{b}_x \quad (\text{A5})$$

$$\frac{d\hat{u}_x}{d\zeta} = \frac{ik\delta T_t}{2\zeta} + \frac{1}{k\delta^2}\sqrt{\frac{\Lambda}{2}}\left(\zeta^2\frac{d^2\hat{b}_z}{d\zeta^2} + \zeta\frac{d\hat{b}_z}{d\zeta} - \hat{b}_z\right) \quad (\text{A6})$$

$$\hat{u}_x = \frac{i}{\delta}\sqrt{\frac{\Lambda}{2}}\zeta\frac{d^2\hat{b}_x}{d\zeta^2} \quad (\text{A7})$$

$$\hat{u}_z = \frac{i}{\delta}\sqrt{\frac{\Lambda}{2}}\zeta\frac{d^2\hat{b}_z}{d\zeta^2}. \quad (\text{A8})$$

After eliminating \hat{b}_x and \hat{b}_z , we find

$$ik\delta\hat{u}_x = -\zeta\frac{d^3\hat{u}_z}{d\zeta^3} \quad (\text{A9})$$

and

$$ik\delta\frac{d^2\hat{u}_x}{d\zeta^2} = \frac{k^2\delta^2T_t}{2\zeta^2} + \zeta\frac{d\hat{u}_z}{d\zeta} + 2\hat{u}_z, \quad (\text{A10})$$

which we combine into a single equation for \hat{u}_z ,

$$\left(\zeta\frac{d}{d\zeta} + 2\right)\left(\frac{d^4}{d\zeta^4} + 1\right)\hat{u}_z = -\frac{k^2\delta^2T_t}{2\zeta^2}. \quad (\text{A11})$$

This equation is equivalent to equation (62), but expressed in terms of ζ . We are interested in the solution of (A11) that matches onto the flow in the weakly magnetic region above, and vanishes in the magnetically dominated region below. These matching conditions can be written as

$$\left. \begin{array}{l} \hat{u}_x \sim u_t + \frac{1}{2}ik\delta T_t \ln \zeta \\ \hat{u}_z \rightarrow w_t \\ \hat{b}_x \rightarrow 0 \\ \hat{b}_z \rightarrow 0 \end{array} \right\} \text{as } \zeta \rightarrow 0 \quad (\text{A12})$$

and

$$\hat{u}_z \rightarrow 0 \text{ as } \zeta \rightarrow \infty. \quad (\text{A13})$$

Conditions (A12) correspond to (61), plus the condition that the magnetic field perturbation vanishes above the transition layer.

After multiplying equation (A11) by ζ , and integrating once, we find

$$\zeta^2\hat{u}_z + \zeta^2\frac{d^4\hat{u}_z}{d\zeta^4} = \text{const.} - \frac{1}{2}k^2\delta^2T_t \ln \zeta. \quad (\text{A14})$$

Using (A9), we can write this as

$$\zeta^2 \hat{u}_z + ik\delta \left(\hat{u}_x - \zeta \frac{d\hat{u}_x}{d\zeta} \right) = \text{const.} - \frac{1}{2}k^2\delta^2 T_t \ln \zeta. \quad (\text{A15})$$

For compatibility with (A12) the constant on the right-hand side must equal $ik\delta u_t + \frac{1}{2}k^2\delta^2 T_t$. We can then use (A6) and (A8) to eliminate $d\hat{u}_x/d\zeta$ and \hat{u}_z from (A15), which leads to

$$\hat{u}_x - u_t - \frac{1}{2}ik\delta T_t \ln \zeta = \frac{1}{k\delta^2} \sqrt{\frac{\Lambda}{2}} \zeta^3 \frac{d}{d\zeta} (\hat{b}_z/\zeta). \quad (\text{A16})$$

The condition that $\hat{b}_z \rightarrow 0$ as $\zeta \rightarrow 0$ implies that the right-hand side of (A16), and hence also the left-hand side, must be $o(\zeta)$. That is, both sides of (A16) must vanish faster than ζ as $\zeta \rightarrow 0$. Similarly, the condition that $\hat{b}_x \rightarrow 0$ as $\zeta \rightarrow 0$ implies that both sides of (A5) are $o(1)$. So we can use (A9) to express all four matching conditions in (A12) as

$$\left. \begin{aligned} \zeta \frac{d^3 \hat{u}_z}{d\zeta^3} &\sim -ik\delta u_t + \frac{1}{2}k^2\delta^2 T_t \ln \zeta + o(\zeta) \\ \hat{u}_z &\sim w_t + o(\zeta) \end{aligned} \right\} \text{ as } \zeta \rightarrow 0. \quad (\text{A17})$$

Equation (A14), with the constant on the right-hand side now identified as $ik\delta u_t + \frac{1}{2}k^2\delta^2 T_t$, becomes

$$\hat{u}_z + \frac{d^4 \hat{u}_z}{d\zeta^4} = ik\delta u_t \frac{1}{\zeta^2} + \frac{1}{2}k^2\delta^2 T_t \frac{1 - \ln \zeta}{\zeta^2}. \quad (\text{A18})$$

We can write the general solution as

$$\begin{aligned} \hat{u}_z &= ik\delta u_t I_1(\zeta) + \frac{1}{2}k^2\delta^2 T_t I_2(\zeta) \\ &+ c_1 \exp\left(\frac{1+i}{\sqrt{2}}\zeta\right) + c_2 \exp\left(\frac{-1-i}{\sqrt{2}}\zeta\right) + c_3 \exp\left(\frac{1-i}{\sqrt{2}}\zeta\right) + c_4 \exp\left(\frac{-1+i}{\sqrt{2}}\zeta\right) \end{aligned} \quad (\text{A19})$$

where c_1, \dots, c_4 are arbitrary constants, and $I_1(\zeta)$ and $I_2(\zeta)$ are the integrals

$$I_1(\zeta) = \int_0^\infty \frac{s ds}{e^{\zeta s}} \frac{1}{1+s^4}, \quad (\text{A20})$$

$$I_2(\zeta) = \int_0^\infty \frac{s ds}{e^{\zeta s}} \frac{\gamma + \ln s}{1+s^4}. \quad (\text{A21})$$

In equation (A21) γ is the Euler–Mascheroni constant,

$$\gamma = - \int_0^\infty e^{-s} \ln s ds = 0.577\dots \quad (\text{A22})$$

The values of the constants c_1, \dots, c_4 are fixed by the matching conditions (A13) and (A17). To determine their values we need to consider the asymptotic behavior of I_1 and I_2 . It can be shown that

$$\left. \begin{aligned} I_1 &\sim \frac{\pi}{4} - \frac{\pi}{2\sqrt{2}}\zeta \\ I_2 &\sim \gamma\frac{\pi}{4} - \frac{\pi}{2\sqrt{2}}(\gamma + \frac{\pi}{4})\zeta \\ \zeta \frac{d^3 I_1}{d\zeta^3} &\sim -1 + \frac{\pi}{2\sqrt{2}}\zeta \\ \zeta \frac{d^3 I_2}{d\zeta^3} &\sim \ln \zeta + \frac{\pi}{2\sqrt{2}}(\gamma - \frac{\pi}{4})\zeta \end{aligned} \right\} \text{ as } \zeta \rightarrow 0 \quad (\text{A23})$$

and

$$\left. \begin{aligned} I_1 &\sim 1/\zeta^2 \\ I_2 &\sim (1 - \ln \zeta)/\zeta^2 \end{aligned} \right\} \text{ as } \zeta \rightarrow \infty. \quad (\text{A24})$$

Matching condition (A13), together with (A24), implies that $c_1 = c_3 = 0$. The remaining matching conditions (A17), together with (A23), then imply that

$$w_t = i\frac{\pi}{4}k\delta u_t + \frac{\pi}{8}\gamma k^2\delta^2 T_t + c_2 + c_4, \quad (\text{A25})$$

$$0 = i\frac{\pi}{2\sqrt{2}}k\delta u_t + \frac{\pi}{4\sqrt{2}}(\gamma + \frac{\pi}{4})k^2\delta^2 T_t + c_2 e^{i\pi/4} + c_4 e^{-i\pi/4}, \quad (\text{A26})$$

and

$$0 = i\frac{\pi}{2\sqrt{2}}k\delta u_t + \frac{\pi}{4\sqrt{2}}(\gamma - \frac{\pi}{4})k^2\delta^2 T_t + c_2 e^{-i\pi/4} + c_4 e^{i\pi/4}. \quad (\text{A27})$$

Solving the three equations (A25)–(A27) fixes the values of c_2 and c_4 , and also imposes a condition on w_t ,

$$w_t = -i\frac{\pi}{4}k\delta u_t - \frac{\pi}{8}\gamma k^2\delta^2 T_t. \quad (\text{A28})$$

The solution for \hat{u}_z is

$$\begin{aligned} \hat{u}_z &= ik\delta u_t \left[I_1(\zeta) - \frac{\pi}{2} \operatorname{Re} \left\{ \exp \left(-\frac{1+i}{\sqrt{2}}\zeta \right) \right\} \right] \\ &\quad + \frac{1}{2}k^2\delta^2 T_t \left[I_2(\zeta) - \frac{\pi}{2} \operatorname{Re} \left\{ (\gamma - i\frac{\pi}{4}) \exp \left(-\frac{1+i}{\sqrt{2}}\zeta \right) \right\} \right]. \end{aligned} \quad (\text{A29})$$

We can also calculate the change in the temperature gradient across the transition layer. This is given approximately by (68), and more precisely by

$$\left[\frac{d\hat{T}}{dz} \right]_{z=-\infty}^{z=+\infty} = \frac{n_{rz}^2}{E_\kappa} \left(\int_{z=-\infty}^{z=+\infty} \hat{u}_z dz - \int_{z=z_0}^{z=+\infty} w_t dz \right) \quad (\text{A30})$$

$$= \frac{n_{rz}^2 \delta}{E_\kappa} \left(\int_0^\infty \hat{u}_z \frac{d\zeta}{\zeta} - \int_0^1 w_t \frac{d\zeta}{\zeta} \right) \quad (\text{A31})$$

$$= \frac{n_{rz}^2 \delta}{E_\kappa} \left(\left(\frac{\pi}{4}\right)^3 \frac{1}{2}k^2\delta^2 T_t - \gamma w_t \right). \quad (\text{A32})$$

B. The global solution, and the vertical flow velocity in the tachocline

As in the work of GB10, we construct an approximate global solution of (22)–(29) by finding the general solution in each region of the domain and then matching these solutions across the boundaries. In our case the boundaries between the regions are at $z = h$ and $z = z_0$, and are known *a priori*, with h given by the background stratification and z_0 given by (44).

B.1. The general solutions in each region

B.1.1. Solution in the convection zone, $z \in [h, 1]$

In the convection zone the governing equations are well approximated by

$$-2\hat{u}_y = -\frac{\hat{u}_x - u_{cz}(z)}{\tau_c} \quad (\text{B1})$$

$$2\hat{u}_x = -ik\hat{p} - \frac{\hat{u}_y}{\tau_c} \quad (\text{B2})$$

$$0 = -\frac{d\hat{p}}{dz} + \hat{T} - \frac{\hat{u}_z}{\tau_c} \quad (\text{B3})$$

$$0 = ik\hat{u}_y + \frac{d\hat{u}_z}{dz} \quad (\text{B4})$$

$$0 = \frac{d^2\hat{T}}{dz^2} - k^2\hat{T}. \quad (\text{B5})$$

The general solution for the temperature perturbation can be written as

$$\hat{T} = a \cosh k(z - 1) + b \sinh k(z - 1) \quad (\text{B6})$$

where a and b are integration constants. From the boundary condition $T = 0$ at $z = 1$ we deduce immediately that $a = 0$. Combining the remaining equations yields

$$\left(\frac{d^2}{dz^2} - \frac{1}{d^2}\right)\hat{u}_z = \left[-\hat{T} + \frac{2i}{k}\frac{du_{cz}}{dz}\right]\frac{\tau_c}{d^2} \quad (\text{B7})$$

where d is the lengthscale defined in equation (51). We write the general solution for \hat{u}_z as

$$\hat{u}_z = -\frac{2i\tau_c}{kd^2} \int_z^1 dz' u_{cz}(z') \cosh\left(\frac{z' - z}{d}\right) - \frac{b}{4\tau_c} \sinh k(z-1) + A \cosh\left(\frac{z-1}{d}\right) + B \sinh\left(\frac{z-1}{d}\right) \quad (\text{B8})$$

where A and B are two additional integration constants. The boundary condition $\hat{w} = 0$ at $z = 1$ implies that $A = 0$. (Since we have neglected the viscous terms in (B1)–(B3) we cannot

impose the stress-free boundary condition at $z = 1$. Including the viscous terms would lead to an Ekman-type boundary layer forming at $z = 1$, but the effect on the solution within the bulk of the convection zone would be of order $E_\nu \ll 1$.)

Finally, the pressure perturbation is found to be

$$\hat{p} = \frac{2i}{k} u_{cz} - \frac{d^2}{\tau_c} \frac{d\hat{u}_z}{dz} \quad (\text{B9})$$

$$= -\frac{2i}{kd} \int_z^1 dz' u_{cz}(z') \sinh\left(\frac{z' - z}{d}\right) + \frac{bkd^2}{4\tau_c^2} \cosh k(z - 1) - \frac{Bd}{\tau_c} \cosh\left(\frac{z - 1}{d}\right). \quad (\text{B10})$$

B.1.2. Solution in the tachocline, $z \in [z_0, h]$

Within the tachocline we have

$$-2\hat{u}_y = 0 \quad (\text{B11})$$

$$2\hat{u}_x = -ik\hat{p} \quad (\text{B12})$$

$$0 = -\frac{d\hat{p}}{dz} + \hat{T} \quad (\text{B13})$$

$$0 = ik\hat{u}_y + \frac{d\hat{u}_z}{dz} \quad (\text{B14})$$

$$\frac{n_{rz}^2}{E_\kappa} \hat{u}_z = \frac{d^2 \hat{T}}{dz^2} - k^2 \hat{T}. \quad (\text{B15})$$

(B11) and (B14) together imply that \hat{u}_z is a constant, $\hat{u}_z = w_t$ say. The remaining equations can then be integrated, and the general solution written as

$$\begin{aligned} \hat{u}_z &= w_t \\ \hat{T} &= \left(T_t + \frac{n_{rz}^2}{k^2 E_\kappa} w_t\right) \cosh k(z - z_0) + K \sinh k(z - z_0) - \frac{n_{rz}^2}{k^2 E_\kappa} w_t \\ \hat{u}_x &= u_t - \frac{1}{2}i \left(T_t + \frac{n_{rz}^2}{k^2 E_\kappa} w_t\right) \sinh k(z - z_0) - \frac{1}{2}iK (\cosh k(z - z_0) - 1) + \frac{in_{rz}^2 w_t}{2kE_\kappa} (z - z_0) \\ \hat{p} &= \frac{2iu_t}{k} + \frac{1}{k} \left(T_t + \frac{n_{rz}^2}{k^2 E_\kappa} w_t\right) \sinh k(z - z_0) + \frac{K}{k} (\cosh k(z - z_0) - 1) - \frac{n_{rz}^2 w_t}{k^2 E_\kappa} (z - z_0) \end{aligned}$$

where u_t and T_t are the values of \hat{u}_x and \hat{T} at the bottom of the tachocline, and K is an additional integration constant.

B.1.3. Solution in the magnetically-dominated region, $z < z_0$

In this region the differential rotation and meridional flow both vanish. The temperature perturbation \hat{T} therefore satisfies

$$0 = \frac{d^2 \hat{T}}{dz^2} - k^2 \hat{T} \tag{B16}$$

$$\Rightarrow \hat{T} = \alpha \cosh kz + \beta \sinh kz. \tag{B17}$$

Since $\hat{T} = 0$ at the lower boundary $z = 0$, we must have $\alpha = 0$.

B.2. Matching conditions

The values of the seven integration constants b , B , w_t , u_t , T_t , K and β are now determined by applying matching conditions across the interfaces $z = z_0$ and $z = h$. At the radiative–convective interface, $z = h$, we impose that \hat{u}_z , \hat{p} , \hat{T} , and $f(z) \frac{d\hat{T}}{dz}$ are all continuous.⁴ These are the same continuity conditions imposed by GB10, except that we use a more realistic thermal energy equation (9), and as a result we require the continuity of the heat flux, rather than the temperature gradient. Across the magnetic transition layer, at $z = z_0$, we impose continuity of \hat{T} and the relations (A28) and (A32) derived from our transition-layer solution.

The matching conditions lead to the following seven relations between the integration

⁴ By imposing that \hat{u}_z is continuous at $z = h$ we neglect any gyroscopic pumping within the overshoot region. This is reasonable provided that the overshoot depth Δ is not too large.

constants:

$$-\frac{2i\tau_c}{kd^2} \int_h^1 dz' u_{cz}(z') \cosh\left(\frac{z'-h}{d}\right) + \frac{b}{4\tau_c} \sinh k(1-h) - B \sinh\left(\frac{1-h}{d}\right) = w_t \quad (\text{B18})$$

$$-\frac{2i}{kd} \int_h^1 dz' u_{cz}(z') \sinh\left(\frac{z'-h}{d}\right) + \frac{bkd^2}{4\tau_c^2} \cosh k(1-h) - \frac{Bd}{\tau_c} \cosh\left(\frac{1-h}{d}\right) = \frac{2iu_t}{k} + \frac{1}{k} \left(T_t + \frac{n_{rz}^2}{k^2 E_\kappa} w_t \right) \sinh kD + \frac{K}{k} (\cosh kD - 1) - \frac{n_{rz}^2 w_t}{k^2 E_\kappa} D \quad (\text{B19})$$

$$-b \sinh k(1-h) = \left(T_t + \frac{n_{rz}^2}{k^2 E_\kappa} w_t \right) \cosh kD + K \sinh kD - \frac{n_{rz}^2 w_t}{k^2 E_\kappa} \quad (\text{B20})$$

$$bk \cosh k(1-h) = \frac{k}{f_0} \left(T_t + \frac{n_{rz}^2}{k^2 E_\kappa} w_t \right) \sinh kD + \frac{k}{f_0} K \cosh kD \quad (\text{B21})$$

$$T_t = \beta \sinh kz_0 \quad (\text{B22})$$

$$Kk = \beta k \cosh kz_0 + \frac{n_{rz}^2 \delta}{E_\kappa} \left(\left(\frac{\pi}{4}\right)^3 \frac{1}{2} k^2 \delta^2 T_t - \gamma w_t \right) \quad (\text{B23})$$

$$w_t = -i\frac{\pi}{4} k \delta u_t - \frac{\pi}{8} \gamma k^2 \delta^2 T_t \quad (\text{B24})$$

where $D = h - z_0$ is the tachocline thickness.

We now seek an explicit expression for the value of the vertical flow w_t within the tachocline. We begin by eliminating B between (B18) and (B19), which leads to

$$\begin{aligned} & \frac{ikd}{\tau_c} w_t \coth\left(\frac{1-h}{d}\right) + \frac{in_{rz}^2 w_t}{k^2 E_\kappa} kD - i \left(T_t + \frac{n_{rz}^2}{k^2 E_\kappa} w_t \right) \sinh kD - iK(\cosh kD - 1) \\ & = 2\bar{u}_{cz} - 2u_t + \frac{ibkd}{4\tau_c^2} \left[\frac{\sinh k(1-h)}{\tanh\left(\frac{1-h}{d}\right)} - kd \cosh k(1-h) \right] \end{aligned} \quad (\text{B25})$$

where \bar{u}_{cz} is the weighted average of the forcing in the convection zone defined by equation (52). The remaining six integration constants, including w_t , therefore depend on $u_{cz}(z)$ only through its average \bar{u}_{cz} . Hence the entire solution below the convection zone is determined by \bar{u}_{cz} .

Next, we combine (B22) and (B23) to eliminate β . The result can then be combined with (B20) and (B21) to express b , T_t and K in terms of w_t . The general result is rather complicated, so for simplicity we describe only two limiting cases, which correspond to the “weakly stratified” and “moderately stratified” regimes identified in §4.1.2.

B.2.1. The weakly stratified regime, $n_{\text{rz}}^2/E_\kappa \ll 1/(k\delta^3)$

In this regime we find that the term in (B23) involving n_{rz} becomes negligible. Since this term arises from the change in the temperature gradient across the transition layer, this regime corresponds to the “weakly stratified” regime described in §4.1.2. After neglecting this term, we find that

$$b = \frac{n_{\text{rz}}^2 w_t}{k^2 E_\kappa} \frac{1 - \operatorname{sech} k(z_0 + D) \cosh kz_0}{f_0 \cosh k(1-h) \tanh k(z_0 + D) + \sinh k(1-h)} \quad (\text{B26})$$

$$T_t = -\frac{n_{\text{rz}}^2 w_t}{k^2 E_\kappa} \frac{f_0 \tanh kz_0 [1 - \operatorname{sech} kD] + \tanh k(1-h) \tanh kz_0 \tanh kD}{f_0 [\tanh kz_0 + \tanh kD] + \tanh k(1-h) [\tanh kz_0 \tanh kD + 1]} \quad (\text{B27})$$

$$K = -\frac{n_{\text{rz}}^2 w_t}{k^2 E_\kappa} \frac{f_0 [1 - \operatorname{sech} kD] + \tanh k(1-h) \tanh kD}{f_0 [\tanh kz_0 + \tanh kD] + \tanh k(1-h) [\tanh kz_0 \tanh kD + 1]} \quad (\text{B28})$$

B.2.2. The moderately stratified regime, $n_{\text{rz}}^2/E_\kappa \gg 1/(k\delta^3)$

In this regime the transition-layer temperature T_t turns out to be smaller than the value given by (B27) by a factor $E_\kappa/(n_{\text{rz}}^2 k\delta^3) \ll 1$. To good approximation, therefore, we can neglect T_t in each of the matching conditions (B18)–(B24), which is equivalent to setting $z_0 = 0$ in (B26)–(B28).

After eliminating u_t between equations (B25) and (B24), and applying the formulae for b , T_t and K just derived, we arrive at an explicit formula for w_t ,

$$w_t = \frac{-i\bar{u}_{\text{cz}}}{\frac{kd}{2\tau_c} \coth\left(\frac{1-h}{d}\right) + \frac{4}{\pi k\delta} + \frac{n_{\text{rz}}^2}{2k^2 E_\kappa} [G_1 + G_2 - G_3]} \quad (\text{B29})$$

where

$$G_1 = kD - \frac{f_0 [2 - 2\operatorname{sech} kD + \tanh kz_0 \tanh kD] + \tanh k(1-h) \tanh kD}{f_0 [\tanh kz_0 + \tanh kD] + \tanh k(1-h) [\tanh kz_0 \tanh kD + 1]} \quad (\text{B30})$$

$$G_2 = \frac{kd}{k^2 d^2 - 1} \left[kd - \frac{\tanh k(1-h)}{\tanh\left(\frac{1-h}{d}\right)} \right] \frac{1 - \operatorname{sech} kh \cosh kz_0}{f_0 \tanh kh + \tanh k(1-h)} \quad (\text{B31})$$

$$G_3 = \gamma k\delta \frac{f_0 [1 - \operatorname{sech} kD] \tanh kz_0 + \tanh k(1-h) \tanh kD \tanh kz_0}{f_0 [\tanh kz_0 + \tanh kD] + \tanh k(1-h) [\tanh kz_0 \tanh kD + 1]} \quad (\text{B32})$$

in the weakly stratified regime, and

$$G_1 = kD - \frac{f_0[2 - 2\operatorname{sech} kD] + \tanh k(1-h) \tanh kD}{f_0 \tanh kD + \tanh k(1-h)} \quad (\text{B33})$$

$$G_2 = \frac{kd}{k^2 d^2 - 1} \left[kd - \frac{\tanh k(1-h)}{\tanh(\frac{1-h}{d})} \right] \frac{1 - \operatorname{sech} kD}{f_0 \tanh kD + \tanh k(1-h)} \quad (\text{B34})$$

$$G_3 \simeq 0 \quad (\text{B35})$$

in the moderately stratified regime.

REFERENCES

- Basu, S., & Antia, H. M. 2003, *Astrophys. J.*, 585, 553
- Bretherton, F. P., & Spiegel, A. E. 1968, *Astrophys. J.*, 153, L77
- Brown, T. M., Christensen-Dalsgaard, J., Dziembowski, W. A., Goode, P., Gough, D. O., & Morrow, C. A. 1989, *Astrophys. J.*, 343, 526
- Brun, A. S., & Zahn, J. 2006, *A&A*, 457, 665
- Charbonneau, P., Christensen-Dalsgaard, J., Henning, R., Larsen, R. M., Schou, J., Thompson, M. J., & Tomczyk, S. 1999, *Astrophys. J.*, 527, 445
- Charbonnel, C., & Talon, S. 2005, *Science*, 309, 2189
- Christensen-Dalsgaard, J., & Schou, J. 1988, in *Seismology of the Sun and Sun-Like Stars*, ed. E. J. Rolfe, vol. 286 of *ESA Special Publication*, 149–153
- Elliott, J. R. 1997, *A&A*, 327, 1222
- Elliott, J. R., & Gough, D. O. 1999, *Astrophys. J.*, 516, 475
- Ferraro, V. C. A. 1937, *MNRAS*, 97, 458
- Garaud, P. 2002, *MNRAS*, 329, 1
- Garaud, P., & Acevedo-Arreguin, L. 2009, *Astrophys. J.*, 704, 1
- Garaud, P., & Bodenheimer, P. 2010, *Astrophys. J.*, 719, 313
- Garaud, P., & Brummell, N. H. 2008, *Astrophys. J.*, 674, 498

- Garaud, P., & Garaud, J. 2008, MNRAS, 391, 1239
- Garaud, P., & Rogers, T. 2007, in *Unsolved Problems in Stellar Physics: A Conference in Honor of Douglas Gough*, ed. R. J. Stancliffe, J. Dewi, G. Houdek, R. G. Martin, & C. A. Tout, vol. 948 of *American Institute of Physics Conference Series*, 237–248
- Gilman, P. A., & Miesch, M. S. 2004, *Astrophys. J.*, 611, 568
- Gizon, L., Birch, A. C., & Spruit, H. C. 2010, *Annu. Rev. Astron. Astrophys.*, 48, 289
- Gough, D. 2000, *Science*, 287, 2434
- Gough, D. O., & McIntyre, M. E. 1998, *Nature*, 394, 755
- Haber, D. A., Hindman, B. W., Toomre, J., Bogart, R. S., Larsen, R. M., & Hill, F. 2002, *Astrophys. J.*, 570, 855
- Kippenhahn, R. 1963, *Astrophys. J.*, 137, 664
- Kosovichev, A. G., Schou, J., Scherrer, P. H., Bogart, R. S., Bush, R. I., Hoeksema, J. T., Aloise, J., Bacon, L., Burnette, A., de Forest, C., Giles, P. M., Leibbrand, K., Nigam, R., Rubin, M., Scott, K., Williams, S. D., Basu, S., Christensen-Dalsgaard, J., Dappen, W., Rhodes, E. J., Jr., Duvall, T. L., Jr., Howe, R., Thompson, M. J., Gough, D. O., Sekii, T., Toomre, J., Tarbell, T. D., Title, A. M., Mathur, D., Morrison, M., Saba, J. L. R., Wolfson, C. J., Zayer, I., & Milford, P. N. 1997, *Sol. Phys.*, 170, 43
- Kumar, P., & Quataert, E. J. 1997, *Astrophys. J.*, 475, L143+
- MacGregor, K. B., & Charbonneau, P. 1999, *Astrophys. J.*, 519, 911
- McIntyre, M. 1994, in *The Solar Engine and its Influence on Terrestrial Atmosphere and Climate*, ed. E. Nesme-Ribes, 293
- McIntyre, M. E. 2007, in *The Solar Tachocline*, ed. D. W. Hughes, R. Rosner, & N. O. Weiss, 183
- Mestel, L. 1953, MNRAS, 113, 716
- Mestel, L., & Weiss, N. O. 1987, MNRAS, 226, 123
- Rogers, T. M., & MacGregor, K. B. 2011, MNRAS, 410, 946
- Rüdiger, G., & Kitchatinov, L. L. 1997, *Astron. Nachr.*, 318, 273
- Rüdiger, G., Kitchatinov, L. L., & Arlt, R. 2005, *A&A*, 444, L53

- Schatzman, E. 1962, *Annales d’Astrophysique*, 25, 18
- Schou, J., Antia, H. M., Basu, S., Bogart, R. S., Bush, R. I., Chitre, S. M., Christensen-Dalsgaard, J., di Mauro, M. P., Dziembowski, W. A., Eff-Darwich, A., Gough, D. O., Haber, D. A., Hoeksema, J. T., Howe, R., Korzennik, S. G., Kosovichev, A. G., Larsen, R. M., Pijpers, F. P., Scherrer, P. H., Sekii, T., Tarbell, T. D., Title, A. M., Thompson, M. J., & Toomre, J. 1998, *Astrophys. J.*, 505, 390
- Spiegel, E. A., & Veronis, G. 1960, *Astrophys. J.*, 131, 442
- Spiegel, E. A., & Zahn, J. 1992, *A&A*, 265, 106
- Strugarek, A., Brun, A. S., & Zahn, J. 2011, *A&A*, submitted
- Thompson, M. J., Toomre, J., Anderson, E. R., Antia, H. M., Berthomieu, G., Burtonclay, D., Chitre, S. M., Christensen-Dalsgaard, J., Corbard, T., De Rosa, M., Genovese, C. R., Gough, D. O., Haber, D. A., Harvey, J. W., Hill, F., Howe, R., Korzennik, S. G., Kosovichev, A. G., Leibacher, J. W., Pijpers, F. P., Provost, J., Rhodes, E. J., Jr., Schou, J., Sekii, T., Stark, P. B., & Wilson, P. R. 1996, *Science*, 272, 1300
- Wood, T. S., & McIntyre, M. E. 2011, *J. Fluid Mech.*, in press (arXiv:1005.5482)
- Zahn, J., Talon, S., & Matias, J. 1997, *A&A*, 322, 320
- Zhao, J., & Kosovichev, A. G. 2004, *Astrophys. J.*, 603, 776

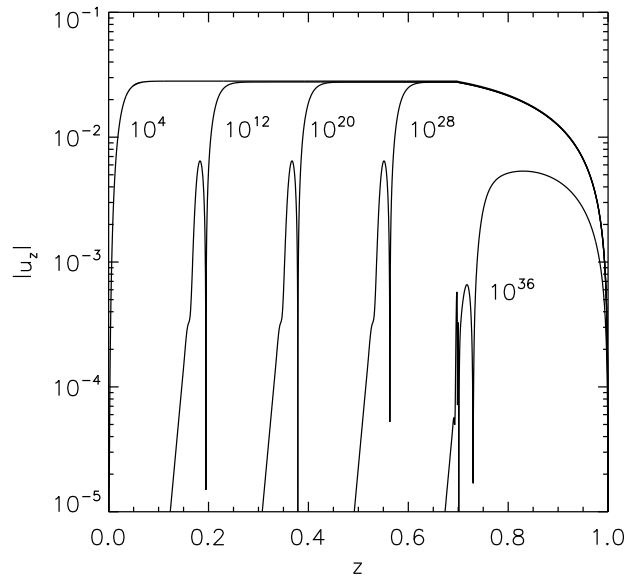


Fig. 4.— Profiles of vertical velocity for a series of unstratified solutions with varying magnetic field strengths. The Elsasser number Λ was increased from 10^4 to 10^{36} in multiplicative increments of 10^8 . Other parameters are as in figure 3. In each solution, the magnetic transition layer is located where the *local* Elsasser number $\Lambda_{\text{loc}} = \Lambda e^{-2z/\delta} \simeq 2/(k\delta)^2$ (see §3.2.1).

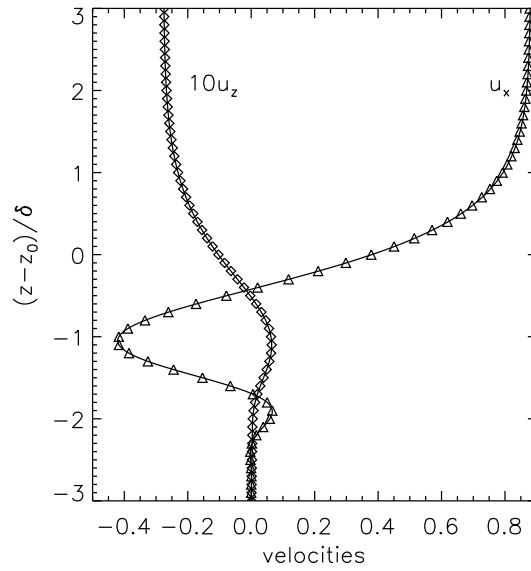


Fig. 5.— The vertical profiles of \hat{u}_z and \hat{u}_x within the magnetic transition layer. The solid lines correspond to the numerical solution shown in figure 3; the symbols correspond to the analytical boundary-layer solution. The \hat{u}_z profile has been multiplied by 10 to make the two profiles visible on the same scale. The vertical axis represents the boundary-layer coordinate $(z - z_0)/\delta$, and so the convection zone lies far above the region plotted.

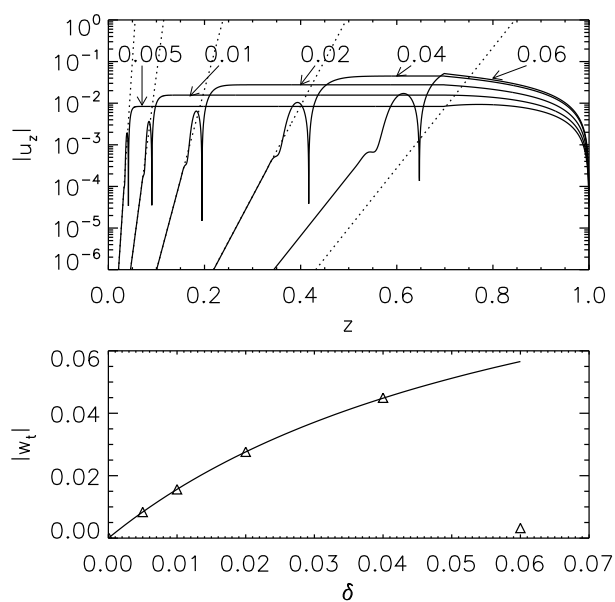


Fig. 6.— Top panel: Vertical velocity profiles for various values of the magnetic scaleheight δ . Other parameters are the same as in figure 3. The dotted lines show the asymptotic behavior (48) of the boundary-layer solution (46) in the magnetically dominated region. Bottom panel: The vertical velocity w_t in the weakly magnetic region predicted by (50). The symbols show the value of \hat{u}_z at $z = 0.65$ in each of the numerical solutions shown in the top panel.

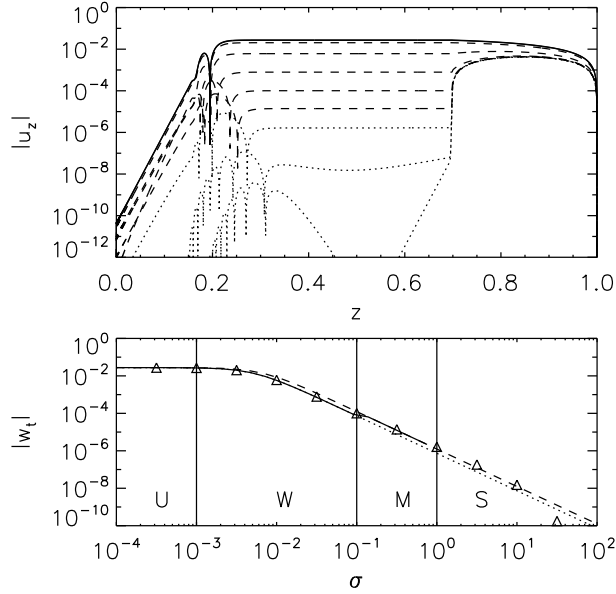


Fig. 7.— Top panel: Profiles of $\hat{u}_z(z)$ from a series of solutions with varying σ . All the solutions have $f_0 = 10^6$ in (20), and the other parameters are the same as in figure 3. We use solid lines for the unstratified solutions ($\sigma = 10^{-5}, 10^{-4}, 10^{-3}$), dashed lines for the weakly and moderately stratified solutions ($\sigma = 10^{-2.5}, 10^{-2}, 10^{-1.5}, 10^{-1}, 10^{-0.5}$), and dotted lines for the strongly stratified solutions ($\sigma = 10^0, 10^1, 10^2$). Bottom panel: The dotted and dashed lines show the vertical velocity w_t in the tachocline predicted by (69) for the weakly stratified and moderately stratified regimes respectively; a solid line is used to indicate the range of σ values in which each is expected to apply. The symbols show the value of \hat{u}_z at $z = 0.5$. The vertical lines indicate the boundaries between the unstratified, weakly stratified, moderately stratified and strongly stratified regimes.

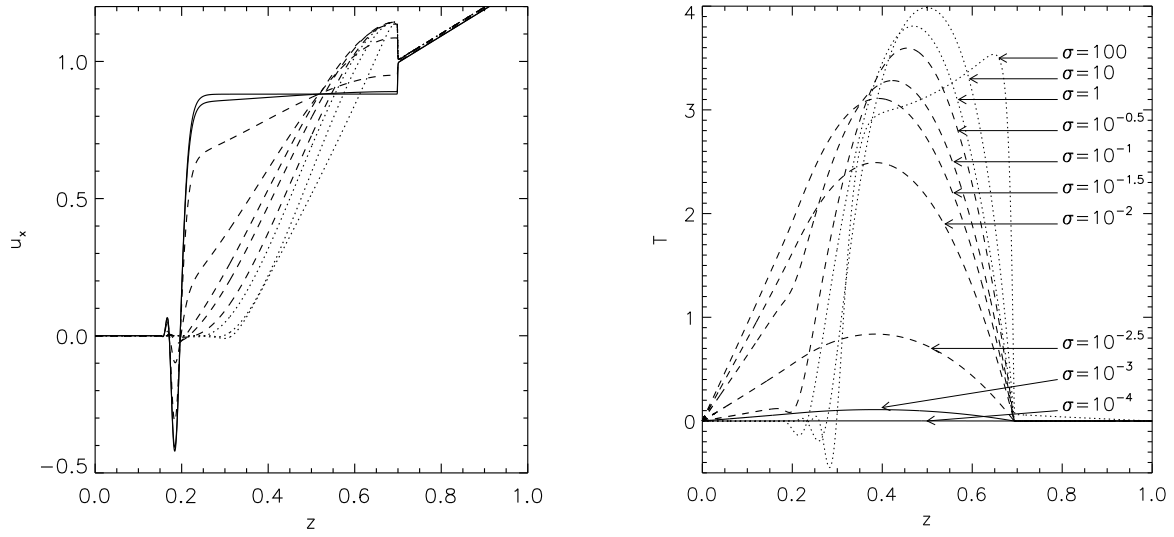


Fig. 8.— Profiles of $\hat{u}_x(z)$ and $\hat{T}(z)$ from the same solutions shown in figure 7. The linestyles are the same as in figure 7. Note that the vertical axes are linear.

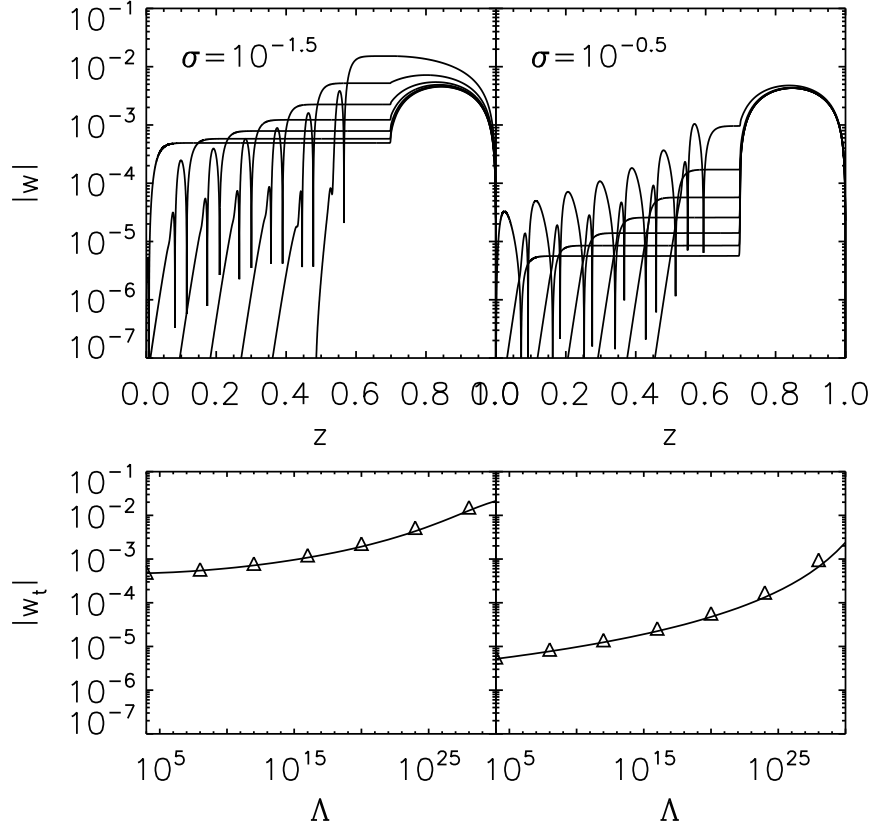


Fig. 9.— Top panel: Profiles of $\hat{u}_z(z)$ from a series of simulations with Λ increasing from $\Lambda = 10^4$ to 10^{28} in multiplicative increments of 10^4 , for $\sigma = 10^{-1.5}$ (left column) and $\sigma = 10^{-0.5}$ (right column). Other parameters are as in figure 7. Bottom panel: The vertical velocity w_t in the tachocline predicted by (69) in the weakly stratified regime (left column) and moderately stratified regime (right column). The symbols show the value of \hat{u}_z at $z = 0.65$, just below the base of the convection zone, for each of the profiles in the top panel.

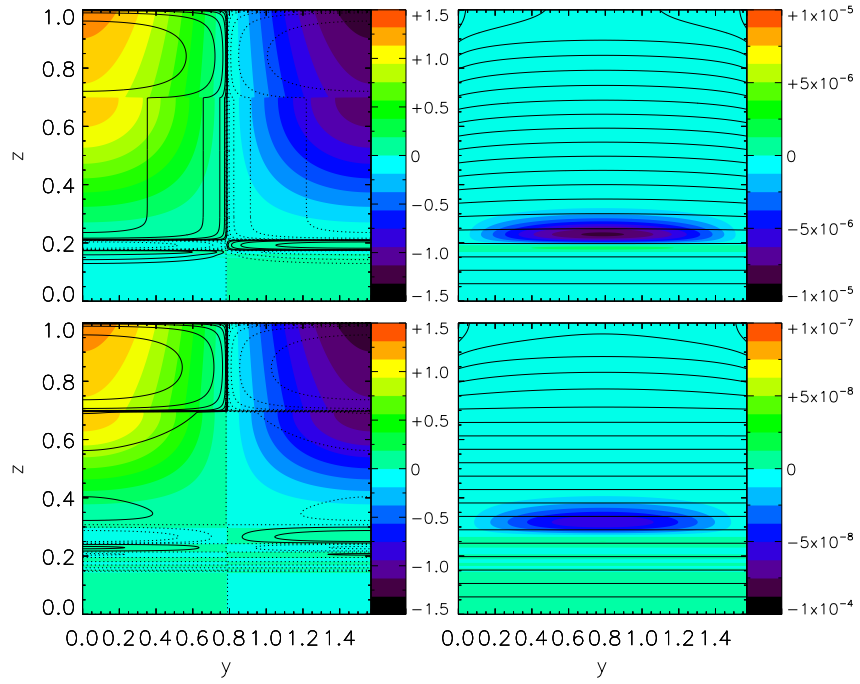


Fig. 10.— Meridional cross-sections through the solutions in figure 7 with $\sigma = 10^{-1.5}$ and $\sigma = 10^2$, corresponding to the weakly and strongly stratified regimes respectively. The left column shows the azimuthal velocity and meridional streamlines. The right column shows the azimuthal magnetic field and poloidal field lines. Different streamlines have been plotted in the two cases because in the strongly stratified regime the meridional flow within the tachocline is weaker by many orders of magnitude.

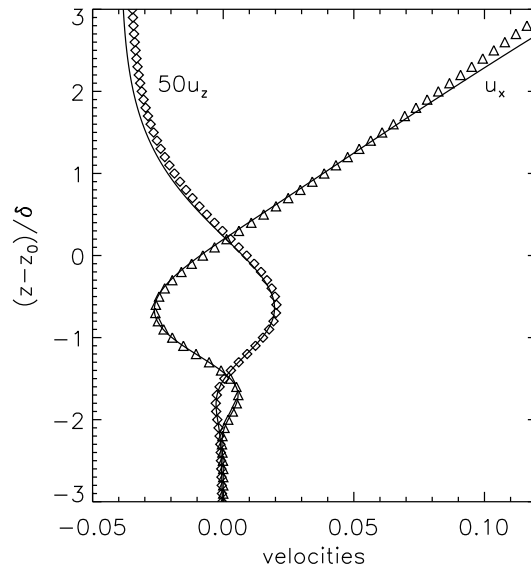


Fig. 11.— The vertical profiles of \hat{u}_z and \hat{u}_x within the tachopause. The solid lines correspond to the numerical solution shown in the top panel of figure 10; the symbols correspond to the analytical boundary-layer solution. The \hat{u}_z profile has been multiplied by 50 to make the two profiles visible on the same scale.